Annu. Rev. Nucl. Part. Sci. 2003. 53:219–61
doi: 10.1146/annurev.nucl.53.041002.110406

DIRECT REACTIONS WITH EXOTIC NUCLEI

P.G. Hansen[1] and J.A. Tostevin[2]

[1]*National Superconducting Cyclotron Laboratory and Department of Physics and Astronomy, Michigan State University, East Lansing, Michigan 48824; email: hansen@nscl.msu.edu*

[2]*Department of Physics, School of Electronics and Physical Sciences, University of Surrey, Guildford, Surrey GU2 7XH, United Kingdom; email: J.Tostevin@surrey.ac.uk*

Key Words One- and two-nucleon knockout reactions, eikonal reaction theory, spectroscopic factors, radioactive ion beams, halo nuclei

PACS Codes 21.10.Jx, 25.70.−z, 25.60.−t

■ **Abstract** The identification of direct-reaction processes and their subsequent exploitation for the spectroscopy of weak radioactive beams of exotic nuclei are important problems in modern nuclear physics. One- and two-nucleon knockout reactions, studied using intermediate-energy radioactive beams, have been shown to be powerful tools for this purpose. This article discusses the current status of such investigations and reviews what has been learned to date from the experiments and analyses of the past five years. The techniques are still in their formative stages, and the open questions and challenges are outlined.

CONTENTS

1. INTRODUCTION

The study of short-lived radioactive nuclei far from the valley of beta stability, often referred to as exotic nuclei, is attracting the interest of physicists worldwide. New experimental methods, now under rapid development, permit studies of the structure of nuclei that lie close to the limits of nuclear existence in the N–Z plane, referred to as the drip lines, where the nucleon separation energy goes to zero. (In order to make the drip line a single-valued function, it is convenient to define the neutron/proton drip lines by the lightest particle-stable nuclide within a family of isotones/isotopes.) Near the neutron drip line, the large neutron excess and low neutron binding energy can lead to dramatic changes in nuclear structure. There is good evidence that for neutron numbers 8 and 20, normally considered to represent "magic" nuclei, i.e., closed-shell structures, the shell gaps disappear at the drip line, and intruder states with opposite parity descend from the next higher shell. These may even become the ground state. In some cases, the low binding allows the wave function of one or more neutrons to extend far beyond the range of the strong force, giving rise to a neutron halo, already observed in a number of light nuclei. Phenomena like these challenge theory and provide a test bench for more exact solutions and an improved understanding of the nuclear many-body problem.

It may be surprising to many that such solutions do not already exist. However, despite many successful insights provided by nuclear structure theory, the existing framework is still largely empirical, and is entirely so for all heavier nuclei. This is because correlations in the wave function brought about by the long-range components of the nucleon-nucleon interaction play a major role. Although the shell model sets out from a picture based on noninteracting nucleons moving in a central field, only a few nuclei, all near double-closed shells, are directly amenable to such a simple approach. The nucleon-nucleon correlations usually make it necessary to take into account explicitly the mixing of many valence configurations. For lighter nuclei, such as those discussed in this article, it is practical to apply a microscopic description that involves diagonalizing a large matrix representing the (effective) interactions in a restricted space of single-particle orbitals. Such techniques have for some time (1) covered nuclei up to mass $A = 40$, and recent developments, such as stochastic methods (2, 3), are now shifting the limit of calculations toward $A = 80$–100 with high predictive power (4). There is also a major current effort to develop accurate ab initio quantum-mechanical calculations using a many-body Hamiltonian derived from the free nucleon-nucleon interaction, as determined from scattering experiments. It is indicative of the difficulty of this task that current technology (see 5 for review) may only be able to handle masses up to approximately $A = 12$.

Nuclear correlations can be probed in a specific and quantitative way by a judicious choice of nuclear reactions that selectively excite some simple degrees of freedom. For example, Coulomb excitation has long been the preferred method for investigating collective degrees of freedom that involve the motion of several or many nucleons. Coulomb excitation has turned out to work extremely well with radioactive beams at intermediate energies of 30–300 MeV/nucleon (6). Perhaps the simplest degree of freedom is that associated with the single-particle orbital components that, at the microscopic level, form the correlated many-body wave function. These can best be studied using direct-reaction processes that add or remove one or a few nucleons and can identify single-particle orbitals, their quantum numbers, and their occupancies. Again it has turned out that reactions with intermediate-energy radioactive beams offer a very powerful tool; these knockout reactions, in which one or more nucleons are removed from the nuclei of the beam, are the subject of this article.

To introduce the subject, we examine in some detail a specific experiment that illustrates how knockout reactions can provide spectroscopic information. The example in Figure 1 is taken from an extensive series of experiments (7–18)

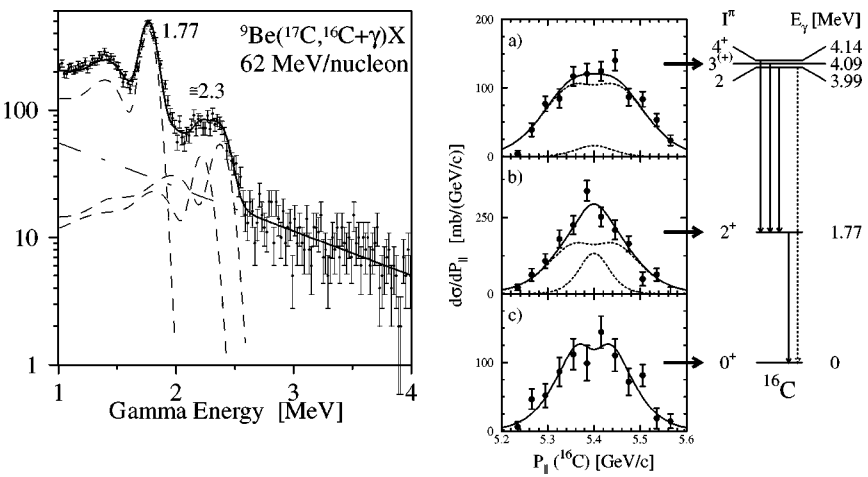

Figure 1 Neutron knockout from a ^{17}C beam. *Left*: Doppler-corrected gamma-ray spectrum observed in the ^{9}Be(^{17}C, ^{16}C + γ)X reaction in coincidence with the reaction residues (12). The solid curve is a fit to the spectrum based on simulated line shapes (dashed lines). *Center*: Diagrams show the parallel-momentum distributions deduced from the γ coincidences, demonstrating that (*a*) and (*c*) are predominantly $\ell = 2$ (the broad components) whereas the cross section to the 1.77-MeV level has an appreciable $\ell = 0$ neutron component (the narrow component). *Right*: A simplified level scheme based on the gamma rays interprets the reaction as feeding (*a*) a group of states near 4 MeV, (*b*) the 2^+ state at 1.77 MeV, and (*c*) the ground state of ^{16}C with cross sections of 33 ± 7, 60 ± 12, and 22 ± 11 mb, respectively.

carried out at the National Superconducting Cyclotron Laboratory at Michigan State University. A detailed analysis demonstrates that the ground state of ^{17}C must have spin parity $3/2^+$ and that the theoretically possible $1/2^+$ and $5/2^+$ assignments are excluded (12). Furthermore, the presence of orbital components of different ℓ in the neutron knockout cross section populating the ^{16}C 2^+ state reveals that the ^{17}C ground state has a complex structure. In simplified language, the main components may be viewed as the $1s_{1/2}$ and $0d_{5/2}$ neutron single-particle states coupled to the first excited 2^+ state of ^{16}C. The deduced $\ell = 0$ and 2 spectroscopic factors for these cross sections are 0.21 ± 9 and 1.2 ± 3, respectively, in good agreement with the shell model that predicts 0.16 and 1.44. (Our definitions and experimental and theoretical details are given later in this article.)

What are the main lessons to draw from this initial example? The first is that the technique is remarkably sensitive; the data in Figure 1 were collected in about one day of measurement with an incident ^{17}C beam of intensity 100–300 particles per second (s^{-1}). The operational limit is considerably lower; in the same series of experiments (12), useful data were taken with a ^{19}C beam of only 0.5–1 s^{-1} (see Figure 3). (Compare this with the 10^{10}–10^{13} s^{-1} beam intensity in a classical cyclotron or Van de Graaf experiment.) Three factors account for this high sensitivity: thick targets of a fraction of a g/cm^2, strong forward focusing due to the high-energy beam, and essentially background-free event-by-event tracking. None of these advantages is present in low-energy experiments with radioactive beams. The second lesson is that the experiment furnishes significant spectroscopic information and thus provides an exacting test, in this case of the structures of the (^{17}C,^{16}C) pair. We consider it crucial that such individual and systematic spectroscopic studies start from a consistent theoretical approach. Case-by-case analyses, each using tailored parameter sets, will be of little value as experiments focus on a few powerful accelerators supplying rare and weak beams. Structure studies must involve a strong interplay between theory and experiment to the benefit of both. The third lesson, to be substantiated below, is that the high-energy limits of reaction theory, based on eikonal methods, offer formal, practical, and quantitative advantages over conventional direct-reaction approaches. This precision offers the possibility of addressing more fundamental problems, such as the physical reality of the orbitals that make up the model space of the shell model.

The organization of this article is as follows. Section 2 gives a brief overview of the applications of direct reactions for nuclear spectroscopy. We also present a brief aperçu of the shell model and spectroscopic factors. We then introduce the single-nucleon knockout reaction, discuss its early applications to halo systems, and present the associated eikonal reaction theory. It is important that the eikonal model provide both a nonperturbative treatment of the projectile breakup mechanisms and an essentially parameter-free estimate of the single-particle knockout cross sections. We use as examples the spectroscopy of bound and unbound final states. In Section 4, we discuss the determination of absolute spectroscopic factors and their relationship to the description and occupation of single-particle orbitals in a truncated model space. This latter question transcends radioactive beam research

and bears on the fundamental basis of the shell model. We then discuss two very recent developments. The first is the observation that two-proton knockout from neutron-rich nuclei and, conversely, two-neutron knockout from proton-rich nuclei must proceed as direct reactions. This opens many new possibilities for structure and two-particle correlation studies in nuclei. The second is that knockout reactions may, in many cases, produce tertiary beams with significant spin alignment. This potentially interesting spectroscopic tool is so far unexplored. Finally, we mention some open questions and experimental and theoretical challenges that will need to be faced in the future.

2. THE LEGACY OF SPECTROSCOPY USING DIRECT REACTIONS

Systematic studies of nuclear reactions were essential to the development of modern nuclear physics. For this review, direct reactions that selectively excite a minimal number of nucleonic degrees of freedom are particularly important. They provide a diagnostic for identifying the microscopic or single-particle structures of nuclei. Unable to cover this vast subject in the space allotted, we present some of the concepts and lessons learned that are especially important to modern experimentation with radioactive beams. We do not address the closely related subject of electromagnetic excitation but point out that the Coulomb excitation of bound states has become an important tool in radioactive-beams research (see 6 for a review). The Coulomb dissociation of simple, loosely bound systems also plays an important role in reactions of halo nuclei and in astrophysics (see 19 and 20 for reviews). Even for reactions on light targets, which are the main concern of this article, in the interest of precision we will often cite the Coulomb-dissociation cross section σ_C in addition to that from the nuclear breakup mechanisms.

2.1. Transfer Reactions

The high resolution offered by cyclotrons and Van de Graaf accelerators permitted the development of a spectroscopy based on direct reactions and the direct measurement of excitation energies of final states. Distorted wave theories of stripping and pickup reactions (21–25), assuming two-body descriptions of both the entrance and exit channels, related the measured fragment angular distributions and nucleon ℓ values of the transfer. The partial cross sections to a given state then lead to spectroscopic factors offering (indirect) information about the single-particle occupancies in the nuclear wave function. The workhorses of this effort were the (d, p) stripping and (p, d) pickup reactions, but many other reactions were used, including two-particle transfers. The role of deuteron breakup effects on the calculated angular distributions and deduced spectroscopic factors was also found to be important (26–29). The adiabatic approach, in particular, clarified (26, 27) that the inclusion of breakup effects reduced the reaction's apparent

sensitivity to the nuclear interior and enhanced its surface localization. Including the effects of breakup greatly improved agreement with theoretical spectroscopic-factor systematics.

The spectroscopic factor is an important quantity that links measurements to microscopic theories of nuclear structure. Detailed discussions of this concept can be found elsewhere (21–23); here we provide a brief definition. Consider the removal of a single nucleon from an initial state of A nucleons of spin I forming a given final state of the $A-1$ nucleon residue with spin I_c. The overlap function between the initial- and final-state many-body wave functions carries angular momentum $|I - I_c| \leq j \leq I + I_c$ and is a function of a single spatial variable. It can be written

$$\left\langle \vec{r}, \Psi_f^{A-1} \middle| \Psi_i^A \right\rangle = \sum_j c_j^{if} \psi_j(\vec{r}), \qquad 1.$$

in terms of an expansion in single-particle states, where details of the angular-momentum coupling are not shown. With the ψ_j normalized to unity, the spectroscopic factor is $\mathrm{S}_j^{if} = |c_j^{if}|^2$. The sum-rule value for the spectroscopic factors to all final states for a specific orbital is the average occupancy of this orbital. Hence, S_j is unity for nucleon removal from a pure single-particle state and $(2j+1)$ for nucleon removal from a filled j subshell. In the isospin representation in which T_i and T_f of the initial and final states are specified, the spectroscopic factor is written $C^2\mathrm{S}$, with C^2 the square of the isospin coupling coefficient. In principle, the one-body overlap functions can be expanded in a complete set of basis states, characterized by different radial quantum numbers n. The notation of Equation 1 is appropriate for most practical shell-model calculations with a space typically restricted to a few j values, each with only one n. When spectroscopic factors are calculated in a harmonic-oscillator basis, they require a center-of-mass motion correction (30). This appears as a factor $[A/(A-1)]^N$, where $N = 0, 1, 2 \ldots$ is the major oscillator quantum number. Often neglected, this c.m. motion correction is important for precise comparisons with data (17, 18).

Comparisons of the theoretical and experimental cross sections for a single-nucleon removal reaction, from initial state i to final state f of the residue, are made assuming

$$\sigma_{\mathrm{th}}^{if} = \sum_j \mathrm{S}_j^{if}\, \sigma_{\mathrm{sp}}(n\ell j), \qquad 2.$$

where the cross sections σ_{sp} are calculated assuming a normalized nucleon-residue wave function ψ_j of given n.

In transfer-reaction analyses, the σ_{sp} are often computed using the distorted-wave Born approximation (DWBA), assuming optical-model two-body entrance- and exit-channel wave functions, or, more recently, by introducing adiabatic or coupled-channels three-body wave functions to include the effects of breakup. For a comprehensive survey of measured spectroscopic factors for the *sd* shell, see Reference (31). Such calculations each involve a significant number of potential

and other parameters that are best chosen (22) from global parameter sets optimized to the systematics for a range of nuclei and beam energies. Such systematics are not available for studies in the neutron- and proton-rich sectors of the nuclear chart.

For reactions with radioactive beams, one must also work with inverse kinematics, since the nucleus of interest is now the projectile and not the target. Interest in the halo nucleus ^{11}Be has prompted work on the $p(^{11}\mathrm{Be},^{10}\mathrm{Be})d$ reaction at 35 MeV/nucleon (32, 33). There are also data for the $d(^{56}\mathrm{Ni},^{57}\mathrm{Ni})p$ reaction (34), but with currently available beam intensities, such experiments are a significant experimental challenge. There is also an interest in applying transfer reactions to investigate (unbound) structures in the continuum. Korsheninnikov et al. (35) used the $p(^{8}\mathrm{He},^{7}\mathrm{He})d$ reaction to observe an excited state in the unbound ^{7}He residue at 2.9 MeV.

Direct proton-transfer reactions have also recently found new applications as an indirect tool for determining the rates of radiative proton capture in certain reactions of interest to nuclear astrophysics. The method makes use of the observation that for a given ℓ, and at large distances from the nucleus, the radial form of the tail of the proton wave function is determined by the asymptotically correct Whittaker function (36). All structure information is therefore in the normalization of this tail, defined by an asymptotic normalization coefficient (ANC) C_ℓ^2 (see 37 and the earlier work cited therein). For a single j value, the C_ℓ is defined by equating the "true" single-particle radial wave function, expressed as the product of structure factors and the normalized radial wave function $R_\ell(r)$, with the product of C_ℓ and the Whittaker function W, the comparison being made at an asymptotic distance r_L. For the general case of a proton with angular momentum ℓ in the oscillator shell N, one has

$$\left[\left(\frac{A}{A-1}\right)^N \mathrm{S}_j\, R_s\right]^{1/2} R_\ell(r_L) = C_\ell\, \frac{W_{-\eta,\,\ell+\frac{1}{2}}(2kr_L)}{r_L}, \qquad 3.$$

where η is the Sommerfeld parameter and k the bound-state wave number. The parameter R_s, to be discussed in Section 4.1, is a correction that reduces the spectroscopic factor and arises from short-range and other correlation effects.

A measurement of the transfer cross section will suffice to determine the ANC and thus specify the proton single-particle wave function at large distances. The method has been applied to proton capture on ^{7}Be (38) and ^{8}B (39) and has been tested in reactions on ^{16}O (40). The method exploits the highly peripheral nature of the transfer reaction at selected energies and fragment angles, thus emphasizing the far nuclear surface. The cross section is then directly correlated with the ANC. Although the deduced asymptotic normalization depends less on the assumed nucleon binding potential than does the spectroscopic factor, comparisons with structure theory are very difficult because the ANC is not an output from most structure calculations. The method also cannot give guidance on the scattering wave function to be used in the calculation of the electromagnetic matrix element, although the choice of nuclear potential can affect the calculated capture rate appreciably (18; S. Typel, unpublished).

The high sensitivity of transfer reactions to the single-particle components in the nuclear wave function requires that the momentum transfer be matched to the momenta of the valence nucleons in the nuclear surface, typically 50–150 MeV/c. This condition is met at tandem energies. An example of what happens at higher energies is provided by a study (41) of the (p, d) reaction at 800 MeV incident beam energy on a number of targets, including ^{12}C and ^{16}O. With momentum transfers in the range 350–500 MeV/c, the single-hole excitations were still seen, but high-spin final states became prominent, and the strongest excitations observed did not correspond to known levels. The authors interpreted these as originating in multistep processes that are favored by the high momentum transfer. This suggests that the adaptation of medium- and high-energy transfer reactions with radioactive beams as a spectroscopic tool may be of limited value for characterizing the wave function, particularly for weakly bound systems. For high-energy one-nucleon knockout reactions, to be discussed in the main part of this article, this problem does not arise; the momentum transferred is that of the struck particle, irrespective of the beam energy.

2.2. Knockout Reactions: $(p, 2p)$ and $(e, e'p)$

Reactions such as $^{16}\mathrm{O}(p, 2p)^{15}\mathrm{N}$ provided an early test of the reality of deeply bound nuclear shell structures. In this case the experiments showed, in addition to the well-known $0p_{1/2}$ and $0p_{3/2}$ hole states at 0 and 6.3 MeV excitation energy, a broad peak near 30 MeV attributed to the $0s_{1/2}$ state [see the reviews (42, 43) of the $(p, 2p)$ reaction]. Using proton beams of several hundred MeV and short wavelength, the reaction has sufficient energy to excite deep-hole states and favors localized interactions, emphasizing single-particle properties. In addition, since the nucleon-nucleon cross sections are small at these energies, the reaction can be treated in the impulse approximation, i.e., as quasifree scattering. The experiments have typically detected the two outgoing protons in coincidence at approximately $\pm 45^\circ$. The proton angular distribution reveals the ℓ value. Near 45°, an s-state has a maximum and a p-state has a minimum. Let the momenta of the incoming and two outgoing protons be $\vec{k}_0$, $\vec{k}_1$, and $\vec{k}_2$, respectively. The excitation spectrum can now be obtained from the momentum balance

$$\vec{k}_{A-1} = \vec{k}_0 - \vec{k}_1 - \vec{k}_2 = -\vec{k}_3, \qquad 4.$$

where $\vec{k}_3$ denotes the momentum of the struck nucleon, which, in the sudden approximation, is equal and opposite to that of the recoiling mass $(A-1)$ residue.

The corresponding proton-knockout reaction using a beam of high-energy electrons has become extremely important for providing absolute spectroscopic factors to test the physical occupancies of the shell-model orbitals. This seemed beyond the powers of nucleon-transfer reactions; thus Macfarlane & Schiffer (22) commented that although transfer reactions could provide relative spectroscopic factors, absolute values were of "very questionable meaning." The $(e, e'p)$ reaction was developed in the 1980s and 1990s into a precision tool for measuring the

spectroscopic factors of proton single-particle states in well-bound nuclei (see especially 44). The results, for deep-hole proton states in nuclei from $A = 6$ to 209, are that the $(e, e'p)$ reaction measures spectroscopic factors that are lower by a factor of 0.50–0.65 than those calculated in the shell model. This systematic reduction is believed to arise from correlation effects, including the repulsive short-range part of the nucleon-nucleon interaction (see 45 for a review). Because hard repulsion sets in at distances below 0.4 fm, it follows from the uncertainty principle that components in the nucleon wave functions must arise with momenta of order 500 MeV/c. These components are hard to measure directly, but lead to reduced occupancies of the low-lying proton single-particle states. The comparison is with shell-model calculations based on effective interactions and model spaces that do not incorporate effects of short-range correlations. A first direct confirmation of this suggestion comes from a study of the ^{7}Li$(e, e'p)^6$He reaction (46). The combined experimental spectroscopic factor to the 0^+ and 2^+ states of ^{6}He was found to be 0.58 ± 0.05, in excellent agreement with the value 0.60 obtained from a microscopic variational Monte Carlo calculation based on realistic nucleon-nucleon interactions.

It now appears that similar information can be obtained for both neutron and proton single-particle states using nuclear knockout reactions, not only for those nuclei available as stable targets but quite generally for all radioactive nuclei available as fast beams. This prospect is discussed in the following section.

3. SINGLE-NUCLEON KNOCKOUT WITH FAST RADIOACTIVE BEAMS

The first experiments with radioactive nuclear beams were carried out more than 50 years ago (47), and the challenging problem of studying the structure of nuclei far from stability was clearly posed by 1966 (48). Nevertheless, the only experimental tools available until the beginning of the 1980s were studies of radioactivity. These included measurements of decay radiation and masses and of ground-state properties (such as spins, nuclear moments, and charge radii) obtained from the atomic hyperfine structure. The emergence of fast radioactive beams from the fragmentation of heavy ions was of major importance to the field and offered the possibility of using nuclear reactions systematically as a tool for studying unstable nuclei. A pioneering step was the estimation of the matter radii of exotic nuclei from interaction cross-section measurements (49). Many such developments of the past decade can be found in a recent volume (50).

At first sight, nucleon-knockout reactions might appear difficult to use, from both experimental and theoretical points of view. We first identify some of the features that make this method such a sensitive, accurate and hence powerful tool.

3.1. General Features of Knockout Reactions

Consider a reaction in which fast, mass-A projectiles with momentum $\vec{k}_A$ have peripheral collisions with a light nuclear target and the mass $(A - 1)$ residues are

detected. If all light fragments remain unobserved, an energy balance is not possible, but the energy of the final state of the residue can be identified by measuring coincidences with its in-flight decay gamma rays. In the sudden approximation, the momentum $\vec{k}_3$ of the struck nucleon in the projectile and that of the residue in the final state, $\vec{k}_{A-1}$, are related by

$$\vec{k}_3 = \frac{A-1}{A}\vec{k}_A - \vec{k}_{A-1}. \qquad 5.$$

It is most convenient in experiments to consider cross-section distributions with respect to a single directional component of the measured momentum. Early work on halos (51) measured the residue distributions as a function of their momentum component transverse to the beam direction. Narrow distributions were observed, associated with the large spatial extent of the neutron halo. In fact, distributions with momentum component parallel to the incident beam are now preferred because these are much less affected by Coulomb deflection and diffractive scattering mechanisms, which are both principally transverse for forward-focused reactions. Measuring longitudinal momentum distributions, however, requires a higher resolution. To estimate the required resolution, consider the physical parameters for the example of an incident radioactive beam of mass $A = 30$ with energy of 80 MeV/nucleon and an exit momentum of around 10 GeV/c. The momentum width (full width at half maximum in one dimension) involved in the creation of a single-particle hole is of order 50–300 MeV/c, the lower limit being typical of a halo state, in which case a resolution considerably better than 0.5% is called for. The stringency of this requirement is clear when it is remembered that the momentum spread of the incident (secondary) beam is much larger, up to 3%, for a beam from a modern fragment separator.

An experiment on ^{11}Li (52) showed that the required resolution can be achieved by operating a spectrograph made of several elements in a dispersion-matched mode. In this mode, the target is located at an intermediate dispersive image plane. The dispersion is then compensated in a second magnetic analyzer, so that the momentum change rather than the absolute momentum is recorded. If, for a neutron removal reaction, the field of the second dipole magnet is reduced by the mass ratio $(A-1)/A$, the spectrometer directly records the distribution, with respect to the quantity k_{3z} of Equation 5, around the central residue momentum. It is instructive to compare this situation with Equation 4 describing the $(p, 2p)$ reaction. There the quantity of interest, often called the missing momentum, emerges as a combination of three measured momenta, whereas the energy-loss method observes it directly despite the poor quality of the secondary fragmentation beam. The close analogy, also with the $(e, e'p)$ reaction, justifies the use of the label "knockout reaction" for all three (see 24).

Much of the work cited below has been carried out with the National Superconducting Cyclotron Laboratory's A1900-S800 spectrometer combination (53). With the incident momentum spread limited to $\pm 0.5\%$, dispersion matching makes it possible to reach a relative momentum resolution of 0.025%. Furthermore, the

high beam energy, 2.4 GeV in the example given above, implies a strong forward focusing so that all reaction residues emerge within a few degrees of the beam direction, well within the angular acceptance of the S800 spectrograph. Essentially all reactions are observed, and the tracking of each individual ion through the spectrometer gives clean and background-free signals. Finally, the coincident detection of in-flight photons emitted from the residues can, after the appropriate Doppler corrections, be used to identify individual final states in the residue and provide partial cross sections and associated residue momentum distributions. (Gamma rays from other sources are revealed by their lack of Doppler shifts.) Here we compare momentum distributions with the theoretical calculations on a relative scale, so that only shapes and widths are compared. These identify the angular-momentum assignments in close analogy with the angular distributions used in the classical low-energy transfer reactions. The absolute scale, expressed as the partial cross section, is then used to extract an experimental spectroscopic factor that relates the structure of the initial and final states.

The high beam momentum permits the use of a semiclassical theoretical description of the reaction in terms of the impact parameter of the relative motion of projectile and target. For the reactions with light targets discussed in this article, the nucleon knockout cross section to a given final state of the residue consists of two contributions. The first component, called stripping or inelastic breakup, accounts for all events in which the removed nucleon reacts with the target and excites it from its ground state. The second component, called diffractive or elastic breakup, describes the dissociation of the nucleon from the residue through their two-body interactions with the target, each being at most elastically scattered. As a result, the removed nucleon is present in the forward beam with essentially the beam velocity, and the target remains in its ground state. These processes lead to different final states, and their cross sections must be added in measurements where only the residue is observed. Elastic breakup due to the Coulomb interactions, called Coulomb dissociation, plays a minor role for the light targets of interest here; however, we include it for precise comparisons. The single-particle cross section can therefore be written

$$\sigma_{\rm sp} = \sigma_{\rm str} + \sigma_{\rm dif} + \sigma_{\rm C}, \qquad 6.$$

where interference between the last two terms has been neglected. Except in the case of halo systems, stripping is usually the dominant nucleon removal mechanism. We do not discuss calculations of $\sigma_{\rm C}$.

The stripping and diffractive cross sections are calculated using eikonal or Glauber theory (54), which has been applied extensively for the interpretation of experiments with radioactive beams (55, 56). The effects of the interactions of the removed nucleon and residue with the target enter the formalism through their phase shifts, which are calculated assuming the fragments each follow a linear trajectory. The treatment of the nucleon, residue, and target three-body system is nonperturbative and contains the effects of projectile breakup to all orders.

The use of reactions on a light absorptive target such as ^{9}Be has several advantages. First, it ensures that the reaction is dominated by the strong interaction and avoids the need for a rigorous simultaneous treatment of both the Coulomb and nuclear excitation mechanisms. Second, the requirement that the residue survives the collision with the target, combined with the highly absorptive character of the residue-target interaction, ensures that nucleon removal must take place from very peripheral projectile impact parameters, leading to strong spatial localization of the reaction at the nuclear surface. The isotope ^{9}Be, with no bound excited states, is an especially good choice because it presents a highly absorptive disk to the incident projectile. The surface dominance is similar but, due to the strong ion-ion absorption, is more complete than is calculated in low-energy transfer reactions, where the light-ion mean free paths determine the surface localization. The early interest in knockout reactions with radioactive beams was motivated by studies of nuclear halo states.

3.2. Nuclear Halo States

Single-particle motion in nuclei is rarely as simple as the extreme single-particle shell model would suggest. As discussed in Section 1, correlations of different physical origins make the description of most nuclear states a complicated matter. The nuclear halo states encountered near the drip lines are to some extent exceptions that bring to mind the hydrogen and helium atoms of atomic physics. Nuclear halos owe their properties to the weak binding of the last nucleon (or nucleon pair), which engenders a wave function with an external tail that extends far outside the nuclear core—the result of quantum-mechanical barrier penetration. Much work has been dedicated to the halo phenomenon since it was first observed (49) and interpreted (57) (see, e.g., 14, 58, 59 and several papers in 60). Examples of single-neutron halos are the ground states of the deuteron, ^{11}Be, ^{14}B, ^{15}C, and ^{19}C. For a neutron halo, it is usually necessary to evaluate radial integrals out to very large distances (40–100 fm). Halos with two neutrons depend on the *n*-*n* interaction for their stability, the best two-neutron halo cases so far being ^{6}He, ^{11}Li, and ^{14}Be. Proton halos are less pronounced because of the Coulomb barrier. Good examples are the $\ell = 1$ proton orbital of ^{8}B, well known for its role in the solar neutrino problem, and the $\ell = 0$ excited level at 495 keV in ^{17}F. Proton halos with $\ell = 0$ are not encountered as ground states until one reaches the light phosphorus isotopes (7, 61), where the $1s_{1/2}$ state fills following the $Z = 14$ proton subshell closure. Here, however, the Coulomb barrier is already sufficiently high that the tails of the halo wave functions are not very pronounced.

The one-nucleon removal reaction experiments on halo states helped to develop the techniques and understanding that led to the more general application of this method, to be discussed in Sections 3.3 and 3.4. Some results are given here; a more detailed discussion, including the process of Coulomb dissociation, can be found elsewhere (14). Early, inclusive measurements of the momentum distribution of residues from halo breakup showed narrow distributions that, from the uncertainty

principle, are expected to be associated with the large spatial extent of the halos. An obstacle to the understanding of halos was the theoretical prejudice that these distributions would simply reflect the square of the Fourier transform of the halo wave function. A closer analysis (62–64) shows that the measurement, in fact, samples the momentum content of the single-particle wave function $\psi_{\ell m}$ only at the nuclear surface and beyond, as was discussed above. A discussion of the early studies of momentum distributions from halo breakup is in Reference (65). A second obstacle was that a considerable fraction of the measured cross sections on single-neutron halo nuclei actually populated excited states of the residue. This implied that the observed inclusive momentum distribution contained broad components superimposed on the narrow distribution associated with the halo state. In the past few years, it has become possible to use gamma-ray coincidences to separate the individual final-state components. Examples of data obtained in this way are the reactions ^{9}Be(^{15}C, ^{14}C $+\gamma$)X (16), shown in Figure 2, and ^{9}Be(^{27}P, ^{26}Si $+\gamma$)X and ^{9}Be(^{19}C, ^{18}C $+\gamma$)X (7), shown in Figure 3.

The use of gamma-ray coincidences for establishing partial cross sections requires an input-output balance of the gamma-ray intensities. This may fail in more

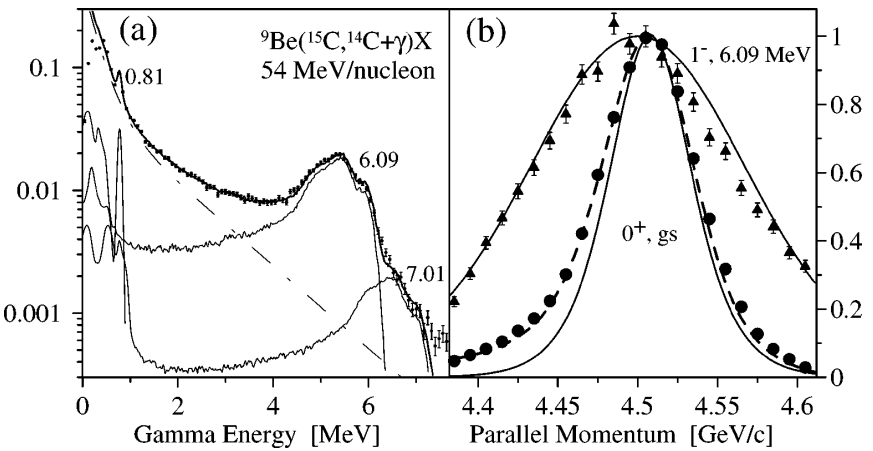

Figure 2 Knockout from the $1/2^{+}$ neutron halo nucleus ^{15}C. The Doppler-corrected gamma-ray spectrum (*a*), observed in coincidence with ^{14}C reaction residues, shows that about 20% of the cross section leads to excited states. The dominant part is to a 1^{-} level at 6.09 MeV with the momentum distribution shown by the triangles in (*b*). Subtraction of the contributions from excited levels gives the momentum distribution of the cross section to the ground state (circles), where the errors are smaller than the size of the points. The solid curves are the parallel-momentum distributions calculated in eikonal theory for $\ell = 0$ and 1. The dashed line is the coupled discretized continuum channel (CDCC) analysis discussed in subsection 3.5. (All distributions are shown in arbitrary normalization. From Reference 16.)

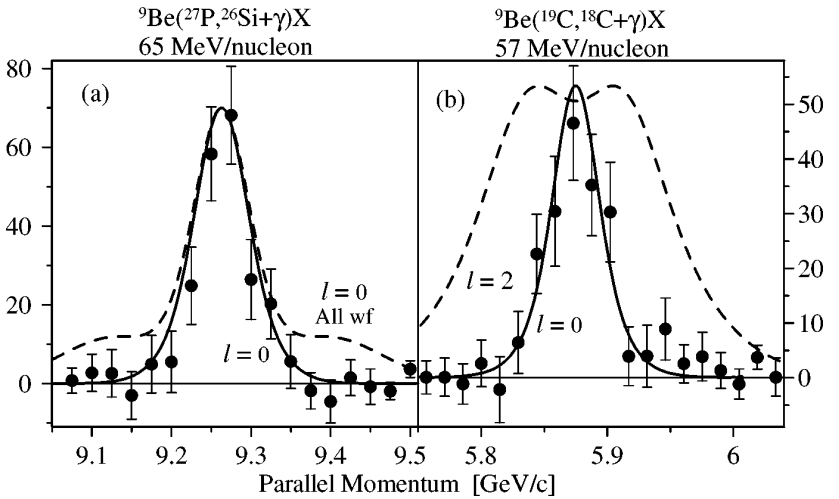

Figure 3 The momentum distributions (7, 12) for knockout to the 0^+ ground states obtained by subtracting the (predominantly $\ell = 2$) distributions to excited state by the method of tagging the coincidences integrally with all gamma rays above 0.25 MeV. The corresponding cross sections relative to the total are $30 \pm 10\%$ for the proton halo of ^{27}P (*a*) and $56 \pm 9\%$ for the neutron halo of ^{19}C (*b*). The curves are theoretical calculations using eikonal theory. (All distributions are shown in arbitrary normalization).

complex decay schemes with many weak and unobserved transitions [see the discussion (66) of the decay of "pandemonium"]. Experiments will show how serious this problem will be; fortunately, it will be small for nuclei at the drip lines, which have very few bound states.

The high-statistics data set obtained in the reaction of ^{15}C, with a $1/2^+$ ground state, clearly identifies an $\ell = 0$ knockout to the ^{14}C ground state and an $\ell = 1$ knockout to the particle-hole state at 6.09 MeV. Figure 2*b* also shows that the differential cross section deviates from eikonal theory, an effect that was also observed in neutron knockout from ^{11}Be (9). In Section 3.5, we discuss the reason for this discrepancy, which apparently is specific to halo states.

In cases where the statistics are too low to permit a detailed analysis of the gamma spectrum, it is still possible to use gamma coincidences as a tag to separate coincident and noncoincident events (7, 12). This works well for ground-state halos, where the subtraction of the coincident events reveals the narrow $\ell = 0$ momentum distributions for the ground-state knockout, as is demonstrated in Figure 3. For the case of ^{27}P, in Figure 3*a*, the dashed line marked "All wf" shows the parallel momentum distribution computed from the Fourier transform of the full radial wave function. The shoulders on this distribution are the high-momentum components due to the inner lobe of the $1s_{1/2}$ wave function. This inner region is not sampled in the reaction and the shoulders are absent from the calculations with

the correct core-target absorption. The *s*-wave cross section to the ground state is 22 ± 8 mb, only 30% of the inclusive value, and translates into a spectroscopic factor of 0.44 ± 0.16 in good agreement with a theoretical value of 0.46. We see that ^{27}P is a complex-structure $1/2^+$ state, far from a clean halo structure.

The example of ^{19}C in Figure 3*b* demonstrates the extreme sensitivity of the high-energy knockout method. The narrow momentum distribution identifies the ^{19}C ground state as mainly $1s_{1/2}$; a *d* assignment would have given a much broader distribution (dashed line). This experiment was carried out with an incident beam with less than one atom of ^{19}C per second (12). Nevertheless, the experiment furnishes a spin assignment, a rough estimate of the neutron separation energy (0.8 MeV), and limits on the spectroscopic factor $S_{1/2} = 0.5$–1.

We now outline briefly the eikonal calculation of the momentum distributions of Figures 1, 2, and 3. The results for the stripping mechanism show very little sensitivity to the details of the absorptive residue- and nucleon-target interactions, so it is possible to simply represent their elastic *S*-matrices by the strong absorption or "black disk" limit. For two bodies, the eikonal approximation (67) leaves the wave function unchanged throughout space, except that it now vanishes within a cylinder with an effective absorption radius. The model is thus geometric with the physical parameter, the black-disk radius, entering through the integration limit. In the case of a composite projectile, there are two parameters, the effective target radius R_T and the minimum impact parameter $b_{\min}$ for a given core impact parameter b. These are chosen to reproduce the empirical nucleon- and residue-target reaction cross sections at the energy of interest. The results can be expressed (63) using cylindrical coordinates as a one-dimensional Wigner transform over the entire z axis, chosen in the beam direction. Explicitly, the differential probability is

$$\frac{\mathrm{d}W_{\ell m}}{\mathrm{d}k_z} = \frac{1}{2\pi} \iiint \psi^*_{\ell m}(\vec{r}_\perp, z')\psi_{\ell m}(\vec{r}_\perp, z)e^{ik_z(z-z')}\mathrm{d}\vec{r}_\perp \mathrm{d}z\ \mathrm{d}z', \qquad 7.$$

where the integration limits are defined in terms of the vector components in the $x - y$ plane and where $|\vec{r}_\perp - \vec{b}| \leq R_T$. As is usual, the cross section involves an integral over impact parameters and sums and averages over all final and initial states, respectively,

$$\frac{\mathrm{d}\sigma}{\mathrm{d}k_z} = \frac{1}{2\ell+1} \sum_m \int_{b_{\min}}^{\infty} \frac{\mathrm{d}W_{\ell m}}{\mathrm{d}k_z}\, \mathrm{d}\vec{b}. \qquad 8.$$

This procedure estimates the momentum distribution for stripping. It is assumed that the distribution for the diffractive mechanism has the same shape. We shall return to this point in Section 3.5.

In these expressions, terms with the maximum value of m are the most important, as can be seen from simple geometrical considerations. Examples are given in Figures 4 and 12. The dominance of extreme-m terms is important for the existence of alignment effects in the cross sections, a subject that we take up in Section 5.

Most of the momentum distributions we show have been calculated using Equations 7 and 8. These approximate (black-disk) expressions also give quite good absolute stripping cross sections, typically within 20–30% of those computed using the more precise formulas to be discussed in Section 3.3.

It is also possible in special cases to derive analytical expressions for the distribution, Equation 7, assuming the single-particle wave functions are sufficiently accurately represented by their asymptotic form. For an $\ell = 0$ neutron halo state, this is a Yukawa wave function defined by the parameter $\kappa = (2\mu S_n)^{1/2}/\hbar$, expressed in terms of the reduced mass and the neutron separation energy. For a target with a large radius, approximated by a planar cutoff, the distribution is (58, 62)

$$\frac{\mathrm{d}W_{00}}{\mathrm{d}x} = \frac{1}{\pi}\frac{1}{(1+x^2)}\,C_1(w), \qquad 9.$$

where the dimensionless x is the momentum k_z in the beam direction measured in units of κ. The expression has the appealing form of the one-dimensional Wigner transform of the entire wave function multiplied by a correction function that can be expressed as a parametric integral,

$$C_1(w) = \int_0^{\pi/2} \cos\theta \exp[-2w/\cos\theta]\,\mathrm{d}\theta, \qquad 10.$$

with $w = (b - R_T)\kappa(1+x^2)^{1/2}$. The effect of $C_1(w)$ is to suppress the unphysical high-momentum components of the one-dimensional Lorentzian, which arise from the singularity of the Yukawa function at the origin. The result shows that the momentum distribution should scale with the dimensionless parameter x. The comparison of the measured momentum distributions for ^{11}Be and ^{15}C is shown in Figure 6 of Section 3.5 and reveals that this scaling holds empirically with great precision.

It is also possible to derive analytic expressions that are valid in the limit of a very small target radius (63). For $\ell = 0$, the two approximations give very similar results, agree with experiments on halo nuclei, and agree with the more realistic calculations based on Equation 7. Expressions for $\ell = 1$ and 2 have also been derived (63, 68) but are of limited value because the use of the asymptotic form is a poor approximation to the actual wave function for non-halo states.

The halo states are, by definition, very close to a continuum threshold and the radial wave function of the least bound nucleon is very sensitive to the actual separation energy. In reactions in which a halo particle is present both before (ψ_1) and after (ψ_2) the reaction, it will be necessary to consider the (radial) mismatch between the initial and final nucleon states due to the change in the average potential. Such a mismatch factor is defined as

$$M = \left| \int d\vec{r}\; \psi_2^*(\vec{r})\psi_1(\vec{r}) \right|^2 \approx \frac{4\sqrt{S_{n1}S_{n2}}}{\left(\sqrt{S_{n1}} + \sqrt{S_{n2}}\right)^2}, \qquad 11.$$

where the right-hand approximation, giving the explicit dependence on neutron separation energies S_{ni}, is based on Yukawa wave functions and hence is appropriate only for *s*-states. The quantity M may be viewed as a small multiplicative correction to our spectroscopic factors, which are obtained from a shell-model description that does not include continuum states. In most cases M is unity, but the correction can be of some importance if the nucleon orbital in the initial or final state is close in energy to a particle threshold. An example of this effect is provided in the (^{12}Be,^{11}Be) single-neutron knockout (10), discussed in Section 3.4. In this case, part of the cross section will be to continuum states above the threshold. There is a clear analogy here to the shake-off effects in atomic physics and to the "ghost states" of nuclear physics (see comments in 14).

3.3. Single-Particle Cross Sections in Eikonal Theory

To provide a more accurate evaluation of the single-particle cross sections arising from the stripping and diffractive breakup mechanisms, we make use of the spectator-core approximation to the many-body eikonal theory. Here core is synonymous with residue, the state of the $A-1$ nucleons that remain after a single nucleon is removed. Such an approach uses more realistic nucleon- and residue-target elastic *S*-matrices than the black-disk approximation of Equation 7. This is essential for a quantitative discussion of deduced spectroscopic factors.

A quite general formal derivation of the inelastic breakup (stripping) cross section is presented by Hussein & McVoy (69) and is also expressed there in the spectator, eikonal limit. The essential step is that the many-body projectile-target system can be reduced to an effective three-body problem, comprising the target, the residue, and the removed nucleon, by use of the spectator approximation—that the $(A-1)$-body residue is at most elastically scattered by the target. In the absence of dynamical excitation, its *S*-matrix with the target is diagonal with respect to core states. The removed nucleon's structure then enters the calculation through the single-particle overlap function ψ_j for the specific A-body initial and $(A-1)$-body final states, discussed in Section 2.1. Using the notation developed above, the stripping cross section can then be written (8, 12, 13, 70)

$$\sigma_{\rm str} = \frac{1}{2j+1}\int d\vec{b}\sum_m \langle\psi_{jm}|(1-|\mathcal{S}_n|^2)|\mathcal{S}_{\rm c}|^2|\psi_{jm}\rangle. \qquad 12.$$

The quantities $\mathcal{S}_{\rm c}$ and $\mathcal{S}_n$ are the elastic *S*-matrices, or profile functions (71, 72), for the residue–target and removed-nucleon–target systems, and are expressed as functions of their individual impact parameters with the target. These can be calculated from empirical potentials, folding approaches, or multiple scattering theory. In the analyses presented, they are calculated using the optical limit of Glauber's eikonal (multiple scattering) theory (54). The nucleon-residue relative-motion wave functions $|\psi_{jm}\rangle$ are calculated as eigenstates of an effective two-body Hamiltonian containing a local potential whose depth is adjusted to reproduce the physical separation energy of the nucleon from the initial state, with given $n\ell j$, to

the residue state of interest. In other words, this energy is the sum of the ground-state nucleon separation energy and the excitation energy of the level. Many calculations have been carried out assuming a fixed Woods-Saxon potential with radius and diffuseness parameters of 1.25 fm and 0.7 fm. We discuss the sensitivity to the choice of these parameters in Section 4. Equation 12 has a simple interpretation. It is the integral over all impact parameters, and average over m substates, of the joint probability of the residue scattering elastically (given by the quantity $|\mathcal{S}_c|^2$) and of the nucleon exciting the target and being absorbed from the elastic channel [given by the quantity $(1 - |\mathcal{S}_n|^2)$].

The form of the corresponding single-particle cross section for diffractive breakup is less intuitive. The diffractive cross section, summed over all continuum relative-motion final states of the nucleon-residue system (13), is

$$\sigma_{\rm dif} = \frac{1}{2j+1} \sum_{\sigma,m} \int d\vec{k} \int d\vec{b} |\langle \psi_{\vec{k}\sigma} | (1 - \mathcal{S}) | \psi_{jm} \rangle|^2, \qquad 13.$$

where we have abbreviated $\mathcal{S} = \mathcal{S}_c \mathcal{S}_n$. Here, consistent with the spectator-core approximation, the continuum breakup states $\psi_{\vec{k}}$ are assumed eigenstates of the same two-body Hamiltonian that initially bound the pair. Completeness of the bound and continuum two-body eigenstates then gives, using closure,

$$\sigma_{\rm dif} = \frac{1}{2j+1} \int d\vec{b} \sum_{m,m'} \left[\langle \psi_{jm} | \, |1 - \mathcal{S}|^2 | \psi_{jm} \rangle \delta_{mm'} - |\langle \psi_{jm'} | (1 - \mathcal{S}) | \psi_{jm} \rangle|^2 \right], \qquad 14.$$

eliminating the need to carry out integration over the continuum. In writing Equation 14, we have also assumed that the spectrum of the two-body Hamiltonian has only a single bound state ψ_j. Although this is clearly an excellent approximation for light halo states, where the ground state is often the only bound state, in general, other bound states will contribute additional terms that must also be subtracted on the right of Equation 14. These off-diagonal bound-state matrix elements take the form of single-particle inelastic excitations that are very small (13) at intermediate energies. Their effect will be to reduce the diffractive cross section calculated using Equation 14.

Reactions in which a weakly bound valence nucleon is present both before and after the reaction, but with significantly different separation energies, were discussed in the preceding subsection in connection with the radial mismatch factors. An additional consideration is in transitions where a more bound nucleon is stripped from a halo nucleus, or one with weakly bound valence nucleons. Such situations arise in the stripping of $p_{3/2}$ and $p_{1/2}$ neutrons from the $1/2^+$ ^{11}Be and ^{15}C ground states, respectively. The reaction residue (core) in such instances is itself a weakly bound composite (8), with an enhanced absorption and reduced survival probability, because of the breakup mechanism with the target. In such cases, the residue should therefore be treated as a composite of a mass $A-2$ core b and a nucleon bound in a state ϕ, and the residue-target S-matrix $\mathcal{S}_c$ calculated

according to Reference (8):

$$\mathcal{S}_c = \langle \phi | \mathcal{S}_b \mathcal{S}_n | \phi \rangle. \qquad 15.$$

For neutron halo states, Equations 12 and 14 make roughly equal contributions to the single-particle cross section. This circumstance is related to the early finding that the total cross section for fast neutrons is approximately twice the geometrical value. An experiment with ^{11}Be, incident at 41 MeV/nucleon on a ^{9}Be target (73), observed the broad angular distribution of the neutrons (out to 20°) expected from the diffractive process. The measured cross section of 120 ± 24 mb was close to half of the inclusive cross section of 290 ± 40 mb, as expected for a pronounced halo state incident on a strongly absorptive target. A new experiment at the GSI-Darmstadt (T. Aumann, personal communication) has determined an elastic-breakup cross section of 26.9 ± 1.4 mb for ^{11}Be at 520 MeV/nucleon on a carbon target. This is in good agreement with theoretical values of 28–32 mb, depending on the particular choice of parameters. (According to theory, 17% of the cross section arises from Coulomb breakup.) For more strongly bound states, the contribution from stripping (Equation 12) is typically a factor of 2–3 greater than that from diffraction (Equation 14). There is actually very little experimental information on the relative roles of the two individual contributions. Enders et al. (18) recently tested the ratio in the case of proton knockout. For ^{8}B, with the results summed over the two populated ^{7}Be final states, they found values of 1.8 (theory) and 2.5 ± 0.9 (experiment) for the stripping-to-diffraction ratio. The corresponding results for ^{9}C were 2.2 (theory) and 2.8 ± 0.9 (experiment). In both instances, the results agree within the experimental errors, but there is perhaps an indication that the diffractive breakup is relatively weaker than predicted by Equation 14.

The essential parameters used in the calculation of the *S*-matrices $\mathcal{S}$ are an effective nucleon-nucleon interaction and the assumed matter distributions, and their root mean squared (rms) radii, of the core and target nuclei. The effective interactions are constructed using the empirical free nucleon-nucleon cross sections (74) and the theoretical real-to-imaginary-part ratios of the forward-scattering nucleon-nucleon amplitudes, as tabulated by Ray (75) for intermediate energies. The effective interaction was assumed to be of zero range for energies above 0.3 GeV/nucleon. For all lower energies, a Gaussian form, of range 0.5 fm, was used (8) that reproduces measured ion-ion reaction cross sections for systems such as ^{12}C-^{12}C and ^{27}Al-^{12}C at 83 MeV/nucleon (76), and the *p*-^{9}Be system at 60 MeV/nucleon (77). The point-particle rms matter radii for many of the reaction residues of interest are now available as measured values [see the review by Ozawa et al. (78)]. Our results are rather insensitive, however, to fine details of the assumed matter radii.

3.4. Examples of Spectroscopy with Knockout Reactions

Accumulating evidence indicates that in neutron-rich nuclei near the drip line the conventional shell gaps associated with the magic numbers disappear and that new gaps corresponding to other subshell combinations appear. As a clear example,

TABLE 1 Spectroscopic factors in the ^{9}Be(^{12}Be,^{11}Be)X reaction* (10)

j^π	E (MeV)	$\sigma_{\rm exp}$ (mb)	M	$\sigma_{\rm str}$ (mb)	$\sigma_{\rm dif}$ (mb)	$\sigma_{\rm C}$ (mb)	$\frac{12}{11}S_j$ exp.	$\frac{12}{11}S_j$ WBT	$\frac{12}{11}S_j$ $0\hbar\omega$
$1/2^+$	0	32.0 ± 4.7	0.79	55.3	24.6	0.8	0.50 ± 0.07	0.61	0.0
$1/2^-$	0.32	17.5 ± 2.6	0.83	36.7	13.0	0.3	0.42 ± 0.06	0.99	2.18
$5/2^+$	1.8	—	—	37.1	12.6	—	—	0.48	0.0

*The calculation of the experimental spectroscopic factors S_j is discussed in the text. We compare them with the shell model results obtained for a closed p-shell (labeled $0\hbar\omega$) and a calculation using the WBT interaction (80). For the latter it was assumed that the lowest $[0p]^8$ and $[0p]^6[1s, 0d]^2$ 0^+ states in ^{12}Be are degenerate (10).

Table 1 shows the case of the $N=8$ nucleus ^{12}Be studied in the ^{9}Be(^{12}Be,^{11}Be $+\gamma$)X neutron knockout reaction (10). The reaction populates the $1s_{1/2}$ ground state and the $0p_{1/2}$ excited state of ^{11}Be at 320 keV, the latter being the only bound excited state in this nucleus. A closed p-shell for ^{12}Be would imply a spectroscopic factor close to 2 for this $1/2^-$ excited level at 320 keV. The gamma spectrum, in coincidence with the ^{11}Be residues, does reveal a strong gamma ray of this energy, but the corresponding intensity and absolute cross section are only one quarter of those expected for the closed shell. Furthermore, the cross section to the $1/2^+$ ^{11}Be ground state is twice as large. This reveals the presence of an important $[1s_{1/2}]^2$ component in the ^{12}Be wave function and shows that the *sd*-shell has already begun to fill appreciably at $N=8$. The measured residue momentum distributions associated with the two states confirm the expected $\ell=0$ and 1 assignments.

The quantitative details shown in Table 1 have been expanded somewhat from the original publication (10) to illustrate more details of the analysis of a knockout experiment. The nuclear single-particle cross sections have been calculated from Equations 12 and 14. The initial state in this case consists of a pair of valence nucleons, one of which is a spectator, and the final-state residues are halo nuclei. This is a case where the few-body composite structure of the residue must be taken into account and the $\mathcal{S}_c$ corrected, according to Equation 15. This correction is small in the case of ^{12}Be compared to the 10%–15% reduction of the single-particle cross sections obtained for the removal of $p_{3/2}$ core-state neutrons from ^{11}Be (8, 9). Relative to a one-body core calculation, based on an rms matter radius of 2.45 fm [the average of the measured values for ^{10}Be and ^{12}Be (78)], the composite-core cross section is lower by about 2% for the *s*-state and higher by about the same amount for the other two states.

For completeness, Table 1 also includes the single-particle Coulomb-dissociation cross section $\sigma_{\rm C}$ (79), which turns out to be negligible. The large difference in neutron separation energies between ^{12}Be and ^{11}Be means that the mismatch factors M, calculated from Equation 11, differ appreciably from unity. The experimental spectroscopic factors are obtained by dividing the measured cross sections by the total $\sigma_{\rm sp}$ and by the mismatch factor M. In this way, the results

can be compared directly with the theoretical spectroscopic factors (10, 80). These include the center-of-mass correction, which those in Reference (10) did not.

The spectroscopic factors to the two final states are both close to 0.5, well below the sum-rule total of 2. The missing components are almost certainly in the $[0d_{5/2}]^2$ configuration, but knockout from this component will lead to the unbound $0d_{5/2}$ configuration in ^{11}Be and therefore cannot be observed in a gamma-ray experiment. This experiment is a direct demonstration of the breakdown of the $N = 8$ shell closure and shows a pairing-type wave function with comparable $[1s]^2 + [0p]^2 + [0d]^2$ components, characteristic of a deformed nucleus. This is especially striking because the even-even ^{14}C neighbor, with eight neutrons, is very magic. (We note for completeness that the fact that the $1s_{1/2}$ intruder is the ground state in ^{11}Be does not permit simple conclusions about ^{12}Be; the measurement shows that the ground state is very different from $[1s_{1/2}]^2$.) The highly deformed character of ^{12}Be finds support in two recent experiments by Iwasaki et al. (81). Using inelastic scattering on a proton target, they find evidence for a strong quadrupole deformation of the neutrons and, on a heavy target, a strong E1 excitation to a 1^- level at only 2.68 MeV. The ^{12}Be experiment also poses the question: Does the neutron halo of the $N = 8$ neighbor, ^{11}Li, also have a significant $0d_{5/2}$ neutron component? This was not considered in the recent experiment on continuum states, which is discussed in Section 3.6.

Other examples are provided by the nuclides ^{15,17}C, shown in Figures 1 and 2. These nuclides are discussed in the original papers (12, 16), which demonstrate the potential of the knockout method for testing both spin assignments and, through the spectroscopic factors, details of the composition of the many-body wave function. The identification and interpretation of the mixed $\ell = 0{,}2$ transition, shown in Figure 1*b*, is a particularly striking example. Although single-nucleon Coulomb dissociation is outside the scope of the present article, it is instructive to compare the knockout analyses with Reference (81a) and also with recent GSI results (82), which studied the same two nuclei using reactions on a lead target. The results clearly demonstrate the selectivity of Coulomb dissociation to *s*- and halo-state components, for which it complements knockout reactions in an interesting way. Coulomb dissociation is likely to be of only limited value for deeply bound or higher ℓ states.

An example of a proton halo state is provided by ^{8}B, in which the proton is bound by only 0.1375 MeV. We return to this nucleus in Section 4.1, in connection with the determination of absolute spectroscopic factors from knockout reactions. The nucleus ^{8}B has been the subject of numerous studies because of its importance for the solar neutrino problem. A recent GSI experiment by Cortina-Gil et al. (83) measured gamma rays in coincidence with ^{7}Be residues and separated the cross sections to the two final states. Figure 4 shows the data, which are in good agreement with calculations based on Equations 7 and 8. An alternative analysis, based on eikonal reaction theory and a cluster model (83), gives very similar results. The dashed lines show the contributions of the $|m| = 0$ and 1 proton magnetic substates to the inclusive spectrum. We note that the contribution from the $|m| = 1$

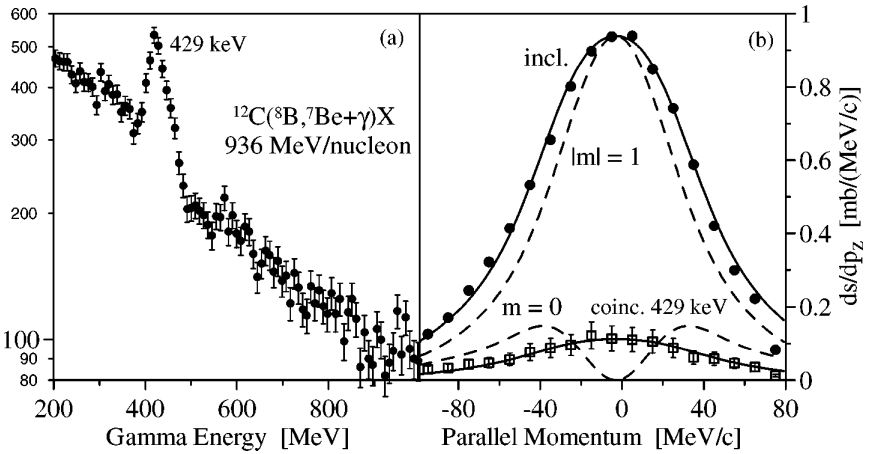

Figure 4 Knockout from the proton halo nucleus ^{8}B at 936 MeV/nucleon (83). The Doppler-corrected gamma-ray spectrum (*a*), in coincidence with the reaction residues, shows that 13±3% of the cross section goes to the ^{7}Be$1/2^{-}$ excited state. The coincident and inclusive momentum distributions (*b*) agree well with the parallel-momentum distributions calculated in eikonal theory for $\ell = 1$, shown as solid lines. The dashed lines show the relative contributions of $|m| = 0$ and 1 to the inclusive spectrum.

components is greater by more than the factor of 2 expected from statistical weights, suggesting a general possibility of alignment effects. This is discussed briefly in Section 5.2.

As a final example, Figure 5 shows residue momentum distributions for the one-neutron knockout on ^{34}Si, which has 20 neutrons. The experiment finds cross section to only three final states (15): the ground state ($3/2^{+}$), a state at 1.01 MeV ($1/2^{+}$), and a state at 4.49 MeV ($5/2^{+}$), corresponding to the three *sd*-shell orbitals. The assignments are clear, although the difference in shapes for the two ℓ values is far less pronounced than for the halo cases of Figures 2*b* and 3*b* because of the relatively high neutron separation energy, 7.54 MeV, of ^{34}Si. (The analogous effect is well known for transfer reactions, where the angular distributions are less distinct for deeply bound states.) The spectroscopic factors S_j of the lowest two states are close to the maximum sum-rule values, $(2j + 1)$, represented by the two points on the extreme right in Figure 5 (*right panel*). This shows that the shell closure at $N = 20$ is preserved in ^{34}Si; this is interesting because the shell gap breaks down for ^{32}Mg with just two fewer protons. Knockout studies on this and other cases in this mass region could map how negative parity intruder states affect the structure as the drip line is approached.

The data in Figure 5 (*left panel*) also invite discussion of the question of the absolute velocities of the residues, which, in the sudden approximation, are equal to the projectile velocity. This is the "no momentum transfer" assumption underlying Equations 4 and 5. The (nominal) beam momentum of the ^{34}Si experiment was

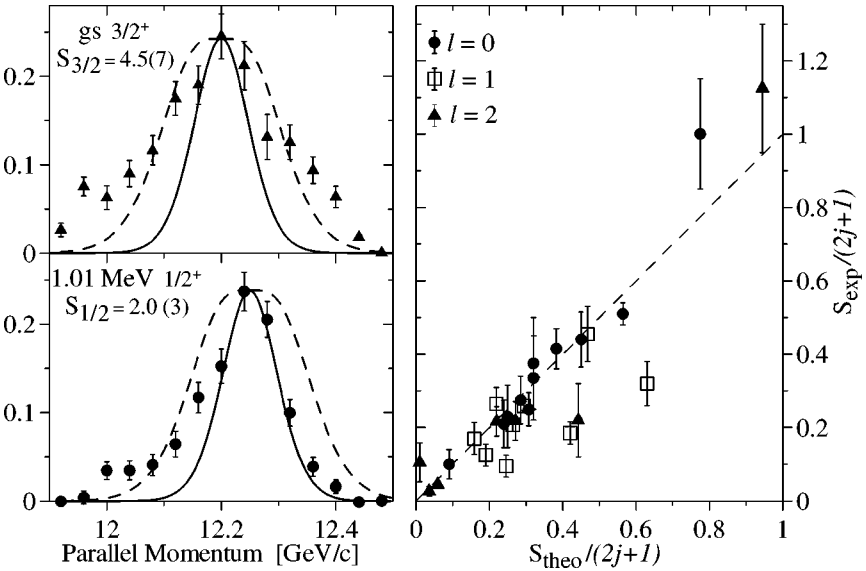

Figure 5 *Left*: Parallel-momentum distributions of the reaction residues in the (^{34}Si,^{33}Si) neutron knockout reaction obtained from gamma-coincidence data (15). Theoretical, eikonal approximation (63) estimates are shown for $\ell = 0$ (solid) and $\ell = 2$ (dashed). The heights and centroids of the theoretical curves have been scaled to match the data. *Right*: Experimental versus theoretical spectroscopic factors in units of the sum-rule value $(2j + 1)$. The dashed line is the diagonal. The two, basically unrelated, quantities are seen to be correlated with a scale factor of approximately unity.

calculated to be 12.270 ± 0.030 GeV/c, in good agreement with the observed peak values for the $3/2^+$, $1/2^+$, and $5/2^+$ states of 12.200 ± 0.004, 12.250 ± 0.003, and 12.250 ± 0.010 GeV/c, respectively, where the errors are statistical only. The fact that the experimental distributions were measured at one setting of the spectrograph and represent subsets sorted on the basis of coincidences with gamma rays permits a more accurate statement about relative momenta because the absolute scale drops out. The distribution associated with the $3/2^+$ ground state is centered at a parallel momentum that is lower than those of the two higher levels by 50 ± 5 MeV/c. A similar effect can be seen in the ^{15}C data of Figure 2*b*, except that in this case it is the excited level that is shifted down by $\sim$8 MeV/c relative to the ground state. The origin of these (small) shifts remains an interesting puzzle. That shifts of opposite sign are obtained for two excited states would seem to rule out a simple connection to energy- and momentum-conservation laws.

To conclude this discussion, we examine how well the spectroscopic factors deduced from the 27 partial cross sections measured so far by the gamma-coincidence method agree with structure theory for the *p-sd* shells. Figure 5 (*right*) shows that the results, expressed in units of the maximum sum-rule value $(2j + 1)$, agree very

well. The four points that are lower than the systematics correspond to states at excitation energies of 6 MeV (in ^{10}Be and ^{14}C) and 4.3 MeV (in ^{33}Si). They may possibly indicate that at these separation energies the single-particle strength is spread more, or differently, than predicted by theory. Alternatively, the cross-section reduction factor of roughly a factor of two could reflect a quenching of shell-model strength associated with effects that we discuss in Section 4.1. The consistency and accuracy of the combination of the shell model and eikonal reaction theory also find support in a series of measurements of inclusive cross sections for 22 nuclides (84). In the absence of gamma coincidences providing partial cross sections, it is necessary to compare the measured cross sections with the sum of all theoretical knockout partial cross sections below the neutron threshold. The results translate into an average ratio of 0.92 ± 0.04 (see 14), in good agreement with the results of Figure 5 (*right*).

3.5. Noneikonal Theoretical Models

Two approximations underpin the eikonal few-body model description of the stripping and diffractive breakup mechanisms discussed in Section 3.3 and exploited above. The first is the adiabatic or sudden approximation—that the projectile energy is sufficiently high, and hence the collision time sufficiently short, that the residue-removed nucleon relative motion can be considered frozen during the collision. The approximation is implicit in Equations 12 and 14, where the reaction *S*-matrices are calculated at fixed impact parameters and then appropriately averaged over all available configurations of the constituents in the projectile. Formally, the approximation to the full three-body model is that, for the purpose of the reaction dynamics, the excitation energy associated with the relative motion of the nucleon and residue is small and is neglected (85). The approximation does not conserve energy and, in particular, does not account for energy transfer between the center-of-mass and relative-motion degrees of freedom of the residue and removed nucleon. The adiabatic condition is well satisfied for collisions on a light target at intermediate energies.

The second is the eikonal approximation. After making the adiabatic approximation one solves the Schrödinger equation assuming the projectile's constituents follow (constant velocity) straight-line paths. It is assumed, therefore, that the elastic *S*-matrices entering Equations 12 and 14 are computed accurately in this limit (54). Calculation schemes that remove one or both of these approximations are available to assess their importance.

One such recent study has been carried out by Esbensen & Bertsch (86), using direct numerical solution of the time-dependent Schrödinger equation to assess the eikonal few-body approach. The time-dependent approach follows the evolution of the nucleon's wave function in the time-dependent potential field it experiences with the target (87). The approach thus does not involve either adiabatic or eikonal approximations for the nucleon motion. On the other hand, the heavy residue's motion is still assumed to follow a simple trajectory with constant velocity and

so is not treated dynamically, and it cannot share energy with the target and nucleon. The analysis shows that the eikonal approximation slightly underestimates the calculated single-particle cross section at all energies, but with a maximum deviation of only 20% at the lowest energy considered, 20 MeV/nucleon. At the energies of the knockout reaction analyses considered here, the deviation is at most a few percent (86). These reduced cross sections of the eikonal model are readily understood, since the eikonal nucleon-target *S*-matrices calculated from potential models have a smaller spatial extent (88), effectively underestimate the size of the target, and underestimate the nucleon-target reaction cross section at low energies. Given the surface dominance of the knockout reaction, both the stripping and diffractive cross-section contributions are also reduced. Calculations that use an exact nucleon *S*-matrix, which is obtained by analytically continuing the partial-wave *S*-matrix and which calculates the correct reaction cross section, are qualitatively and quantitatively very close (89) to the noneikonal calculations of Reference (86).

A closely related treatment of the reaction is provided by the transfer-to-the-continuum (TC) approach of Bonaccorso & Brink (90), developed from the semiclassical transfer model of Hasan & Brink (91). Once again the nucleon's motion is allowed to evolve with time, and the adiabatic and eikonal approximations are not made. In addition, by assuming the residue follows a straight-line path and that the final-state interactions of the nucleon and the residue can be neglected, one avoids the need for a time-dependent solution, and much of the calculation can be carried out analytically. However, an important additional approximation required to enable the analytic reduction is that only the (Hankel function) asymptotic form of the nucleon-core initial bound state and of the nucleon-target final-state wave function (the *S*-matrix) are involved. Although this will be a reasonable approximation for the neutron halo states, this approximation is not quantitative for more bound and non-*s*-state transitions, as was discussed in the context of the analytic formulae for the momentum distributions in Section 3.2. Nevertheless, an interesting prediction of this model is that for $\ell = 2$ transitions, the linear and angular-momentum matching conditions involved in the nucleon's transfer between the residue and the target lead to momentum distributions with a marked asymmetry (92). This prediction has yet to be confirmed experimentally with data of sufficient statistics. In cases where the eikonal and TC model predictions for the σ_{sp} have been compared directly (e.g., 15, 93), the agreement is very good.

Recently (16), the coupled discretized continuum channels (CDCC) method (28, 29) has also been used to investigate the accuracy of the eikonal method. CDCC proceeds by constructing a square-integrable basis of relative motion states in the separation of the projectile constituents on which to expand the three-body wave function of the projectile and target. Using this basis, CDCC approximates the three-body problem by an effective two-body coupled-channels equation set. Unlike the methods discussed above, the CDCC solves the full three-body problem without approximating the three-body dynamics. To date, CDCC has been used to calculate only the diffractive-breakup part of the knockout reaction. The

calculations (see Table I of Reference 16), confirm that the integrated diffractive single-particle cross sections of the eikonal model are reliable. CDCC also permits the study of more precise features of the data, such as the observed low-momentum tail on the measured parallel momentum distributions for the ground-state–to–ground-state transitions in ^{11}Be and ^{15}C (9, 16) (see also Figure 2). By definition, the momentum distributions are symmetric (see Figure 2), within the eikonal model.

Details of CDCC, of the calculation of the breakup triple differential cross sections, and of the parallel momentum distributions of the residues can be found in References (94) and (16). For breakup of the ^{11}Be and ^{15}C halo systems on a ^{9}Be target at 50–70 MeV/nucleon incident energies, breakup energies up to 30 MeV and relative-motion partial waves up to *g*-waves were needed in the neutron-residue system. Such values are rather universal, reflecting the linear and angular-momentum transfer induced by the surface diffuseness of the constituent-target nuclear tidal interactions.

Figure 2*b* shows the measured momentum distributions for the ^{15}C beam of 54 MeV/nucleon. The solid curves are the eikonal calculations. The dashed curve, which includes the CDCC calculation of the elastic breakup component, gives an excellent description of the measured asymmetry of the ground-state momentum distribution. The agreement with the ^{11}Be data is of equal quality. We attribute this agreement to our correct treatment of the continuum, of the flux excited, and of the reduction in energy available to the residues. To date, this effect has been observed experimentally only for halo states, which is consistent with the large diffractive cross-section component in these cases.

The details of the distributions in Figure 6*a* are now fully understood and can be reproduced with high accuracy. This being the case, Figure 6*b* now adjusts the momentum scale for the ^{11}Be data, according to the ratio of the ^{15}C and ^{11}Be separation energies, $\sqrt{1.218/0.503}$, to test the scaling property discussed following Equation 10. It is clear that the data sets are essentially identical upon scaling, reflecting the universal character of the distribution, including the low-momentum tail, for these halo systems.

3.6. Knockout to Continuum States

It is a much more delicate matter to apply direct reactions to study nuclei with no bound states. We take as an example the $N = 7$ isotones, where ^{11}Be marks the neutron drip line. Here, single-particle states in the systems located one and two steps beyond the drip line, $^{9}\mathrm{Li} + n$ and $^{8}\mathrm{He} + n$, have both been studied in direct reactions. Especially for the *s*-states, which are not expected to show a resonant behavior, the ideal approach would be to measure the phase shifts from neutron elastic scattering as a function of energy. However, even though both nuclei and neutrons are available as beams, none is available as a target. An alternative is to investigate final-state interactions in the decay spectra of the unbound residual nuclei (here, ^{10}Li and ^{9}He) formed in direct one- and two-proton knockout reactions

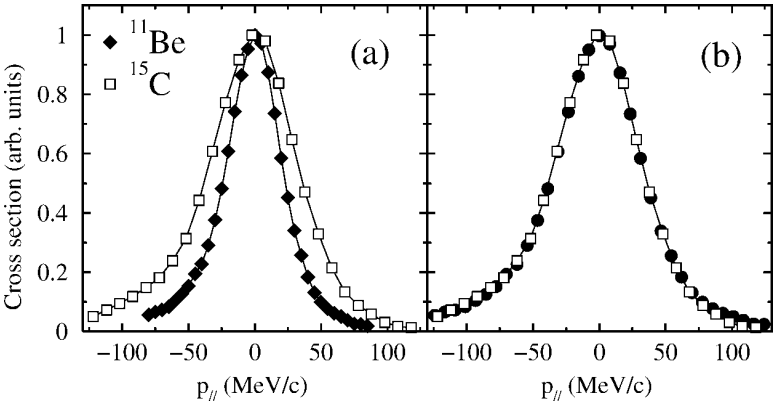

Figure 6 Comparison of (*a*) the measured parallel momentum distributions, in the projectile rest frame, for the ground-state–to–ground-state transitions in neutron removal from ^{11}Be (solid diamonds) and ^{15}C (open squares) at energies of 54 and 60 MeV/nucleon, respectively (16). The lines are a guide to the eye. In (*b*) the filled circles show the result of scaling the width of the ^{11}Be distribution by the square root of the ratio of the separation energies, $\sqrt{1.218/0.503}$, an illustration of the scaling relationship discussed in connection with Equations 9 and 10.

from ^{11}Be (95, 96). Because the valence neutron in ^{11}Be is predominantly in a $1s_{1/2}$ state, these reactions will have a favorable spectroscopic strength to an $\ell = 0$ neutron final state. Both show a strong final-state interaction in the $\ell = 0$ channel indicative of a low-lying *s*-state. The strength of this neutron interaction is best parameterized in terms of the neutron scattering length a_s, with $|a_s|$ found to be large in both cases: For ^{9}Li + *n*, $a_s < -20$ fm, and for ^{8}He + *n*, $a_s < -10$ fm. This suggests that the $1/2^+$ virtual states are the ground states of ^{10}Li and ^{9}He. This is expected from the level systematics of the $N = 7$ isotones, based on data from References (95, 97–99) and (100) (see Figure 7 and Reference 101).

The momentum distribution of the $(A - 2)$ residue in the breakup of a two-neutron halo is a long-standing problem. Simon et al. (102) have demonstrated how to approach it. They reconstructed the combined momentum distribution of the ^{9}Li + *n* residue that is formed in stripping a neutron from ^{11}Li on a light target. The ^{9}Li + *n* momentum represents the quantity $\vec{k}_{A-1}$ in Equation 5 and is related to the momentum distribution of the stripped neutron in the same way. The measured momentum distribution could be resolved into approximately equal contributions from $[1s]^2$ and $[0p]^2$ components. An even more striking signature was obtained in that experiment by observing the angular correlation of the decay products from the recoiling ^{10}Li (Figure 8). The strong forward-backward asymmetry observes directly the interference between the $\ell = 0$ and 1 final states. Similar experiments have been carried out for ^{6,8}He (103).

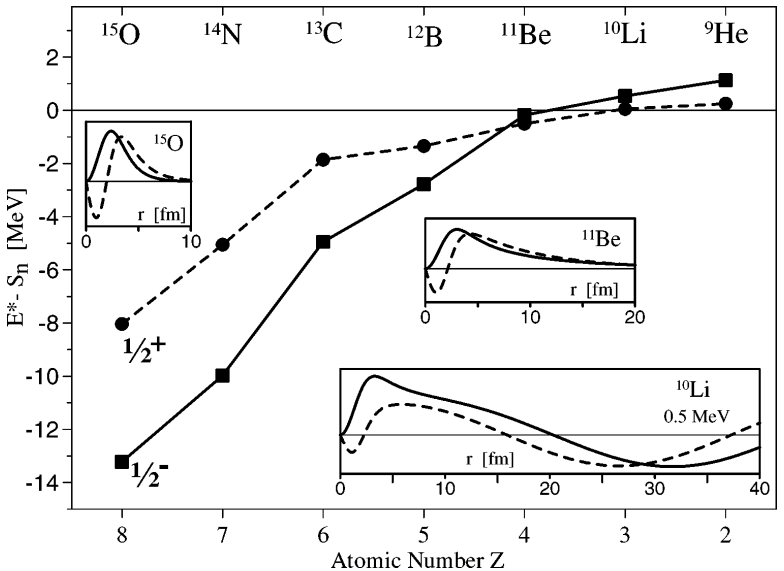

Figure 7 Systematics of the eigenenergies (101) of the $1/2^+$ (circles, dashed curves) and $1/2^-$ (squares, solid curves) states as a function of the proton number for the $N = 7$ isotones. The effective single-particle energy is taken as the difference between the nuclear excitation energy and the ground-state neutron separation energy. In ^{15}O with one neutron hole in the 8-8 doubly-closed shell, the $1/2^+$ state belonging to the next (*sd*) shell is 5 MeV above the $1/2^-$ ground state. The two states approach each other with decreasing proton number. In ^{11}Be they have crossed so that the $1/2^+$ intruder is the ground state, and the *s* and *p* states are bound by only 0.50 and 0.18 MeV, respectively. Both are halos with radii close to 7 fm. (The core radius is 2.3 fm.) The same states have been observed (95, 97–100) as continuum states in the unbound nuclei ^{10}Li and ^{9}He. The insets show the calculated single-particle wave functions $\chi(r) = r\,R(r)$ against *r* calculated for a Woods-Saxon potential. Both states are deeply bound with spatially well-localized wave functions in ^{15}O; they are halos in ^{11}Be and continuum wave functions in ^{10}Li (shown for a kinetic energy of 0.5 MeV) and ^{9}He. Reproduced with permission from Elsevier.

4. ABSOLUTE SPECTROSCOPY AND SHORT-RANGE CORRELATIONS

Very recently, work has been done to assess whether the one-nucleon knock-out reaction can provide accurate absolute occupancies of orbitals in the valence shell (17, 18). These initial studies suggest that it can. If this holds true as more experimental evidence becomes available, it will allow a more systematic exploration of the foundations of the shell model, incorporating data for both neutron and proton orbitals. Experimentation with radioactive beams will also allow

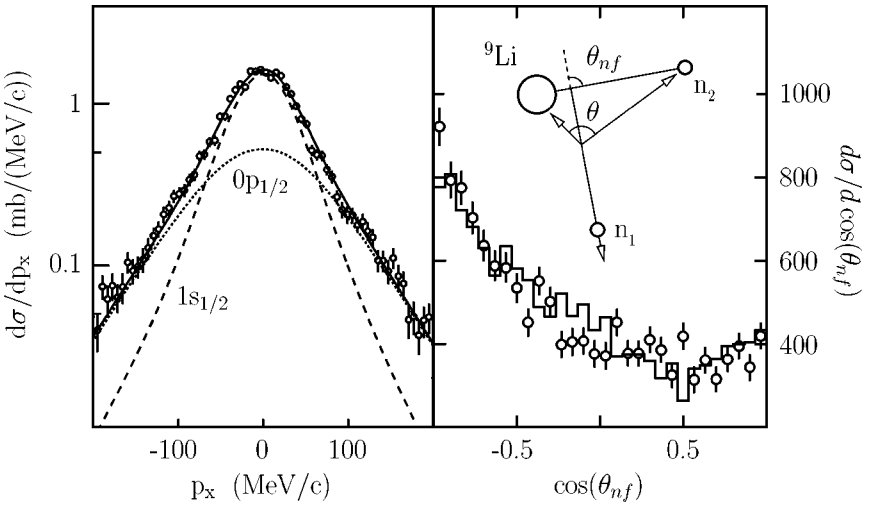

Figure 8 *Left*: ^{10}Li residue momentum distributions measured following neutron removal from ^{11}Li on ^{12}C at 287 MeV/nucleon. *Right*: Angular correlations of the decay neutrons measured relative to an axis defined by the ^{10}Li recoil direction as shown in the inset. The points are the experimental data and the histogram is a reconstruction corrected for experimental resolution and acceptance effects. Note the strong forward-backward asymmetry, which reflects interference of the $\ell = 0$ and 1 final states. (From Reference 102 with permission.)

the study of loosely bound states in very unstable systems, such as nuclear halo states.

The wider perspective is that data of this kind may reveal the contributions from correlations in the single-particle motion arising from effects not normally included in a shell model with effective interactions. For simplicity we refer to these as short-range correlation effects, but spin-dependent interactions associated with the tensor force, and possibly other phenomena, will also enter. This was the subject of the earlier discussion, in Section 2.2, of the $(e, e'p)$ reaction, which has been considered uniquely able to access absolute spectroscopic factors. Here, in addition, we present the (still limited) evidence for the use of knockout reactions for determining the asymptotic normalization coefficients of single-particle wave functions, an application recently suggested by Trache et al. (104). In this connection, we assess the likely precision with which spectroscopic factors and asymptotic normalization coefficients can be obtained from these surface-dominated direct reactions.

4.1. Quenching Factors R_s from Knockout Reactions

Several papers have attempted to analyze how well measured cross sections agree with the theory outlined in Section 3. For the set of about 25 measured partial cross sections, most for weakly bound nucleons in the *p-sd* shells, a first survey (14, 15)

found that a plot of the deduced experimental spectroscopic factor versus that of theory (the shell model) had a strong correlation with most but not all points close to the diagonal (see Figure 5, *right*). However, in many cases the experimental errors are large and the theoretical values sensitive to the precise choice of parameters.

Brown et al. (17) and Enders et al. (18) carried out a more exacting comparison by selecting cases where the structure is well studied and well understood, such as ^{16}O and ^{12}C as well as the radioactive ^{8}B and ^{9}C. For these cases, accurate inclusive cross-section data, good to ≈5%, have also been taken over a wide range of energies—for the ^{8}B case from 0.08 to 1.44 GeV/nucleon. This range tests that the spectroscopic factor is extracted consistently; furthermore, the eikonal model is at its most reliable at high energies. Several refinements improved the accuracy of the analysis. The rms radii of the projectile cores and the target were taken from experiment. In the earlier systematic studies (14), the wave functions describing the nucleon-core relative motion were calculated in a Woods-Saxon potential with a "standard" set of radius and diffuseness parameters $r_0 = 1.25$ fm and $a = 0.7$ fm. For the test cases discussed here, it was possible to use optimized values based on experiment or, in the case of ^{15}C, on a self-consistent Hartree-Fock calculation. For each of the three projectiles discussed in the present work, analyses exist that permit the selection of such an optimized set. Use of the "standard" set does not change the conclusions appreciably.

Under the assumption that a considerable portion of the correlations arising from the long-range part of the nuclear force are included in the shell-model spectroscopic factors S_j^{th}, we define an empirical reduction factor,

$$R_s = \frac{S_j^{exp}}{S_j^{th}}, \qquad 16.$$

for a partial cross section with a single j value. For an analysis of an inclusive knockout cross section, the average R_s can be defined as the ratio of the cross section to the sum of the theoretical cross sections to all states that lie below the nucleon threshold (see 17).

The results of the analyses for the cases where the nucleons are strongly bound are shown in Figure 9. The effective separation energies here cover the range 10–19 MeV. The results for protons, of 0.5–0.65, are in good agreement with those from $(e, e'p)$ reactions (44). The results for neutrons, which could not be obtained in electron-scattering experiments, are very similar, as would be expected from isospin symmetry. The physical occupancies are much lower than those suggested by shell-model calculations. A completely different picture emerges for the data taken with loosely bound, halo-like states, shown in Figure 10. In these cases, the R_s factors are 0.8 to 0.9, which may explain why the first analyses, discussed above, find little quenching of the spectroscopic factors. This interplay of long- and short-range correlations clearly poses an interesting challenge to theory and to experimentation with radioactive beams in the years to come.

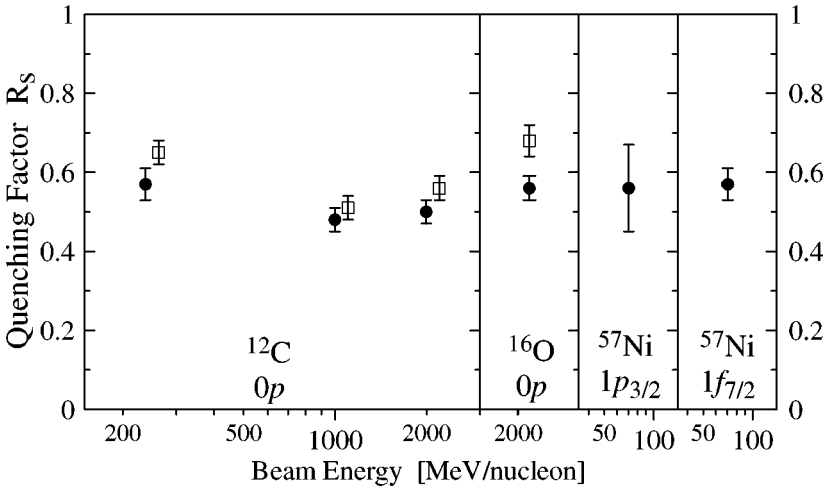

Figure 9 Systematics of the reduction factor R_s, attributed to short-range correlations, for the isotopes ^{12}C and ^{16}O (17) based on data from References (105) and (106) and for ^{57}Ni. (K.L. Miller, unpublished). The reactions leading to the final states have nucleon separation energies in the range 10–19 MeV. The open squares are the results for proton knockout; the full circles are for neutron knockout. The ^{57}Ni experiment used a beryllium target, whereas the other experiments used a carbon target. The measurements, except for the $1p_{3/2}$ state of ^{57}Ni, are inclusive.

4.2. Experimental Sensitivity to Single-Particle Orbitals

Nuclear astrophysics studies often need absolute cross-section information in an energy range that is not directly accessible to experimentation. For radiative capture reactions, an essential quantity of interest is the large-distance behavior of the bound-state wave function; the continuum single-particle wave function is assumed to be better understood. One recent paper (37) starts from the assumption that knockout reactions furnish precise absolute occupancies, a viewpoint that finds support in the results presented in Section 4.1. From Equations 2 and 3, and the definition of R_s (Equation 16), we can obtain an expression for the asymptotic normalization coefficient

$$C_\ell^2 = \frac{\sigma_{\rm exp}}{(\sigma_{\rm str} + \sigma_{\rm dif} + \sigma_{\rm C})} \left(\frac{r_L \; R_\ell(r_L)}{W_{-\eta,\, l+\frac{1}{2}}(2kr_L)} \right)^2, \qquad 17.$$

where a possible contribution from Coulomb dissociation has been included. This expression is conveniently insensitive to specifications of nuclear-structure parameters and illustrates why the asymptotic normalization coefficient can be obtained with somewhat higher precision than the spectroscopic factor (37). The essential point is that the square of the single-particle wave function and the

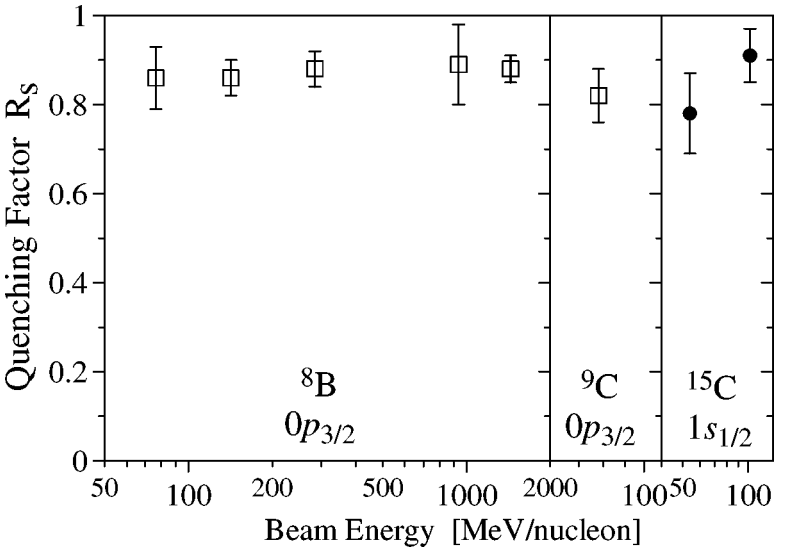

Figure 10 Systematics of the reduction factor R_s, attributed to short-range correlations, for the isotopes ^{8}B (17) (with data from References 83 and 107–109), ^{9}C (18), and ^{15}C (J.R. Terry, unpublished). The final states have nucleon separation energies in the range 0.14–1.3 MeV. Open squares represent the results for proton knockout; solid circles are for neutron knockout. The ^{15}C experiment used a beryllium target, the others carbon targets. The measurements for ^{8}B are inclusive, but a recent experiment (83) found that the branch to the ^{7}Be excited level is $13 \pm 3\%$, in agreement with the theoretical calculation (see Figure 4).

theoretical cross sections are correlated. We examine this question further below. The technique has been applied to deduce the asymptotic normalization of proton wave functions for the ^{8}B and ^{9}C nuclei (17, 18, 37, 104). The results are consistent with measurements by other methods.

Knockout reactions sample the nucleon wave functions near the nuclear surface. Information deduced on absolute spectroscopic factors must therefore involve an extrapolation to take account of the interior parts of the wave function. We can estimate the fraction of the wave function observed by the ratio of the single-particle stripping cross section to the free-nucleon reaction cross section with the target. For a pronounced halo system such as the $1s_{1/2}$ neutron state of ^{11}Be, with a separation energy of 0.503 MeV, this fraction is close to 50%, whereas for ^{15}C, with a neutron separation of 1.218 MeV, the fraction is 30%. The $0p_{3/2}$ state of ^{8}B is only a moderate proton halo despite a separation energy of only 0.1375 MeV (the effect of the Coulomb barrier) with a fraction of about 25%. For a deep hole state such as the $0p_{1/2}$ neutron in ^{12}C, bound by 18.7 MeV, the fraction detectable at 250 MeV/nucleon is only 12%.

The errors arising from the implicit extrapolation can be estimated from Equations 2, 12, and 14. Evaluating partial derivatives of the spectroscopic factors with respect to the Woods-Saxon potential parameters in a finite-difference approximation, one obtains for some of the cases above

$$^{15}\mathrm{C}:\ \delta(\mathrm{S}_j)/\mathrm{S}_j = -0.40\,\delta r_0 - 0.81\,\delta a$$

$$^{8}\mathrm{B}:\ \delta(\mathrm{S}_j)/\mathrm{S}_j = -0.52\,\delta r_0 - 0.96\,\delta a,$$

where the coefficients are given in fm^{-1}. These suggest errors of 2%–10%. Deeply bound core states are mainly sensitive to r_0, with a coefficient of order -1.2. The values chosen for r_0 and a are normally correlated; this effect can be examined by choosing the rms radius r_{rms} and a as the independent variables. This leads to

$$^{15}\mathrm{C}:\ \delta(\mathrm{S}_j)/\mathrm{S}_j = -0.41\,\delta r_{\mathrm{rms}} - 0.025\,\delta a$$

$$^{8}\mathrm{B}:\ \delta(\mathrm{S}_j)/\mathrm{S}_j = -0.43\,\delta r_{\mathrm{rms}} - 0.004\,\delta a.$$

With these variables, the spectroscopic factors are independent of a, and an error of 0.1 fm on the radius leads to a 4% error on the spectroscopic factor. The determination of the asymptotic normalization coefficient benefits from correlated factors in the numerator and denominator to give, for the case of ^{8}B,

$$^{8}\mathrm{B}:\ \delta(C_\ell^2)/C_\ell^2 = 0.24\,\delta r_0 + 0.59\,\delta a,$$

a factor of 2 more precise than the relative spectroscopic factor.

5. NEW DEVELOPMENTS

5.1. Two-Nucleon Knockout as a Direct Reaction

Bazin et al. (110) show evidence that two-proton removal reactions from neutron-rich nuclei proceed as direct processes. The basic reason is that the alternative process of one-proton knockout followed by proton evaporation is strongly suppressed relative to gamma decay and neutron evaporation from the intermediate states. This is brought about by the asymmetry in proton and neutron separation energies; for the example below, the proton channel from ^{27}Na only opens up at excitation energies above 13.3 MeV. The technique for observing this process is basically the same as that for one-nucleon removal reactions, discussed in Section 3.4. Figure 11 shows the momentum distribution of the residues and the coincident gamma-ray spectrum obtained for the reaction ^{9}Be(^{28}Mg,^{26}Ne)X. From the point of view of nuclear structure, this is a fairly transparent example because the reaction connects two spherical *sd*-shell nuclei, which are stabilized by the pronounced $N = 16$ subshell closure (3).

Direct reactions involving two particles differ fundamentally from one-particle reactions. For single-nucleon knockout in the sudden approximation, discussed

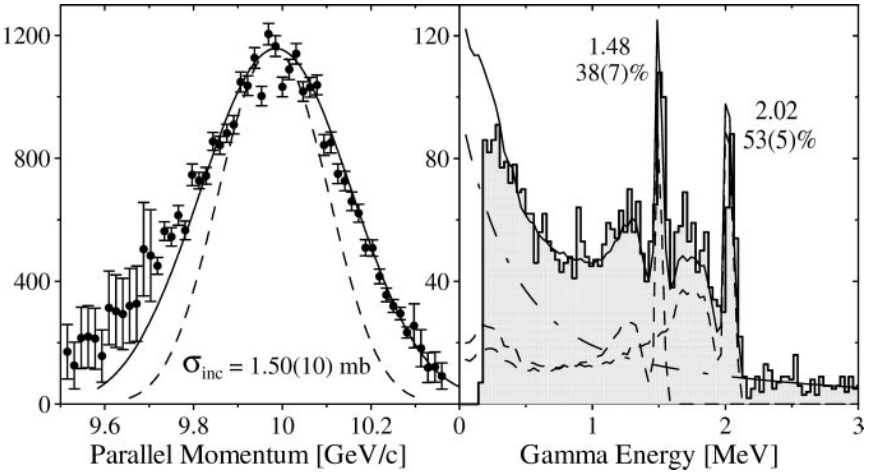

Figure 11 *Left*: The parallel-momentum distribution for the inclusive two-proton knockout reaction from ^{28}Mg. The theoretical curves, discussed in the text, include the broadening that arises from the difference in stopping power in the target for projectile and residue. The solid curve is the estimate for knockout of two protons in 0*d*-states, whereas the dashed line is for two protons in 1*s*-states. *Right*: The gamma-ray spectrum (in units of counts per 32-keV/bin). The main peaks are labeled by the energy in MeV (error 0.02 MeV) and by the absolute intensity relative to the number of observed fragments. The dashed peak shapes are simulated response curves normalized to match the number of counts in the full-energy peaks. The continuous distribution (dot-dashed line) is attributed to radiation from the target, and the sum of the three is shown as a solid curve. The 1.48-MeV and 2.02-MeV peaks are interpreted as originating from the 4^+ and 2^+ levels of ^{26}Ne, respectively.

in Section 3, and for single-nucleon transfer reactions, the theoretical cross sections often factorize as a product of reaction dynamics and structure terms. This convenient feature does not generalize to reactions involving two nucleons. In two-nucleon knockout (and two-particle transfer reactions), the transition amplitudes for a given total angular-momentum transfer J are now a coherent superposition of many contributing pair combinations. The transition amplitudes thus mix inextricably the dynamical and structural aspects.

Bazin et al. (110) noted important differences between two-nucleon knockout and two-particle transfers. In the latter, the transfer vertices impose selection rules that often dictate that the nucleon pair must transfer as a spin-singlet–isospin-triplet. Such selection rules do not operate for the knockout reaction, and any configuration of the pair of particles in the valence shells can contribute. It is then possible to start from the assumption that the two particles are uncorrelated, except for those spatial correlations implicit through their binding to a common core. Eikonal reaction theory (8) then suggests that the basic unit of cross section, neglecting spin-orbit splitting for simplicity, is

$$\sigma_{\ell_1\ell_2} = \int d\vec{b}\,|\mathcal{S}_c|^2 \prod_{I=1,2} \frac{1}{2\ell_i+1} \sum_{m_i} \langle \ell_i m_i | (1-|\mathcal{S}_{pi}|^2) | \ell_i m_i \rangle, \qquad 18.$$

the two-nucleon analogue of Equation 12. $\mathcal{S}_{pi}$ and $\mathcal{S}_c$ are, as usual, the elastic *S*-matrices for the removed-nucleon–target and the residue–target systems. The proton-residue relative-motion wave functions $|\ell m\rangle$ are once again calculated in a Woods-Saxon potential whose depth is adjusted to reproduce the observed proton separation energies. The recoil of the heavy residue is neglected. Diffractive breakup processes are assumed to be negligible for neutron-rich systems with very deeply bound proton states.

For two-proton removal from the *sd*-orbitals of ^{28}Mg, these elementary cross sections are $\sigma_{22} = 0.29$ mb, $\sigma_{00} = 0.35$ mb, and $\sigma_{20} = 0.32$ mb. (In addition to the uncertainty introduced by the approximation, it should be kept in mind that for deeply bound states the absolute spectroscopic factors discussed in Section 4.1 are reduced by the factor $R_s = 0.5$. We may expect to encounter similar effects in the two-proton reaction.) To convert the theoretical unit cross sections into a two-nucleon knockout cross section, one must define the appropriate spectroscopic amplitudes. Within the extreme independent-particle approximation, it follows from simple combinatorics that, for p particles in the valence shell, the factor multiplying the pair cross sections is $S_p = p(p-1)/2$. For ^{28}Mg, with $p = 4$, the calculation based on σ_{22} then gives 1.8 mb, in good agreement with the measured inclusive cross section of 1.50 ± 0.10 mb given in Figure 11. This strongly supports the direct-reaction interpretation.

A second check of this interpretation comes from the shape of the parallel-momentum distribution of the residues shown in the left part of Figure 11. The relatively narrow parallel-momentum distribution centered close to beam velocity is, qualitatively, the signature of a direct reaction. A more quantitative interpretation requires, in principle, the differential equivalent of Equation 18. The task of calculating this may, however, be simplified by our earlier observation that this distribution probes the wave function's momentum content only in the surface of the nucleus, and that this quantity changes only slowly with the distance from the core. The distribution for two independent particles is then, to a good approximation, given by folding those for two independent nucleons. The solid theoretical curve in the left part of Figure 11 was obtained in this way and lends further support to the interpretation of the reaction as a direct knockout of two protons from the $0d$ orbital. We expect that the shapes of the momentum distributions for two-proton removal will be of less value as a diagnostic tool than the one-nucleon process because each J channel will mix several ℓ values. This will make the shapes less characteristic.

The calculation of spectroscopic strength to individual final states requires a more detailed model. In their first analysis, Bazin et al. (110) assume that the four valence protons in ^{28}Mg are restricted to the $0d_{5/2}$ subshell. The possible final states of ^{26}Ne are 0, 2, and 4^+, which have spectroscopic factors 4/3, 5/3, and 3, respectively, and which sum to the inclusive value $S_p = 6$ given above. Dividing the approximate partial cross section obtained from Figure 11 by the unit cross section σ_{22}, Bazin et al. obtain (in the same order) 2.4 ± 0.5, 0.3 ± 0.5, and 2.0 ± 0.3 in

semiquantitative agreement. The low cross section to the 2^+ level presents a problem in this very simple model. If, on the other hand, shell-model wave functions are used, and the two protons are restricted to a relative 0*s*-state configuration, a pronounced reduction in the $J = 2$ channel, and spectroscopy in agreement with the experiment (110) is obtained. This calls to mind the "fingerprints" characteristic of one- and two-nucleon transfer reactions on complex nuclei (111).

The reaction and its mirror, the two-neutron knockout on proton-rich nuclei, are very promising tools for spectroscopy of exotic nuclei. They lead directly toward nuclei whose yield is extremely small in the direct production process. We expect that the cross sections will provide specific and quantitative information on nuclear structure. Furthermore, the method should be applicable over a wide mass range. We note in this context that our example, ^{28}Mg, is closer to stability (^{32}S) than it is to the drip line (^{22}C).

5.2. Alignment Effects and Gamma-Ray Angular Distributions

As was mentioned in Section 3.2, the surface character of the single-nucleon knockout reaction is reflected in the observed momentum distributions in a characteristic way, described approximately by Equation 7. For single-particle angular momenta $j > 1/2$, the cross sections also depend on the individual m substates, leading to nuclear alignment. In this section, we discuss some possible consequences and future applications of this effect. These have yet to be studied experimentally.

The magnitude of the alignment effect is illustrated in Figure 12*a* for a single-neutron $\ell = 2$ knockout with theoretical single-particle cross sections of 12.5, 11.6, and 26.0 mb for states with $m = 0$, 1, and 2, respectively. The unaligned, spin-averaged cross section is 17.6 mb. This m sensitivity suggests that, in experiments where the secondary beam has spin greater than $1/2$ and was produced in a breakup process, it is entirely possible that some degree of spin alignment will be present in the beam. This could be a source of systematic error on the absolute cross section. With this in mind, an exploratory theoretical study was carried out for the spin-$3/2$ ^{17}C system at 65 MeV/nucleon (112). It showed that the calculated analyzing powers T_{20} associated with the stripping process could indeed be significant. For an incident beam of alignment t_{20}, the cross section due to the aligned beam is

$$\sigma_{\rm sp}(\text{aligned}) = \sigma_{\rm sp}\,[1 + t_{20}T_{20}]\,, \qquad 19.$$

where $\sigma_{\rm sp}$ is the usual, unaligned single-particle cross section. $T_{20}(0^+)$ for the pure $\ell = 2$ ^{16}C ground-state transition was found to be 0.234 within the eikonal model. In the case of the mixed ℓ transition to the ^{16}C 2^+ state (see Figure 1), the calculated analyzing power is also of order 0.2. Furthermore, due to interference of the $\ell = 0$ and 2 contributions (112), $T_{20}(2^+)$ is sensitive to both the sign and the magnitude of the assumed admixtures. There is, as yet, no experimental evidence that bears on these questions, but they will provide a rich and necessary field for future studies.

Tertiary beam alignment will also manifest itself through a nonisotropic emission of gamma rays from the reaction residues. As a specific example, consider

neutron knockout from the 0^+ ground state of ^{28}Mg producing the $5/2^+$ state at 1.7 MeV in ^{27}Mg. To lowest order, the m_ℓ population of the residue will then correspond to the single-particle knockout cross sections calculated from Equations 7 and 8. If we transform these to the j alignment and use the expressions given in the reviews by Yamazaki (113) and, with special emphasis on fragmentation reactions, by Stuchberry (113a), the theoretical angular distributions of gamma rays can be calculated. The results for the two examples in Figure 12*b* show that the anisotropy is expected to be appreciable. It can be increased further by cuts in the momentum distribution. The cross-hatched area in Figure 12*a* includes 38% of all events, but the anisotropy is then doubled. It is clear that the method has great potential for identifying the spins of residues and the associated gamma-transition multipolarities in knockout reactions.

The additional scale on the abscissa of Figure 12*b* illustrates the strong effect of the Lorentz boost in a fast-beam knockout reaction. This can easily be incorporated in the analysis and does not, in principle, present any obstacle. The strong forward peaking implies that the angular detection range 0°–60° will yield the highest count

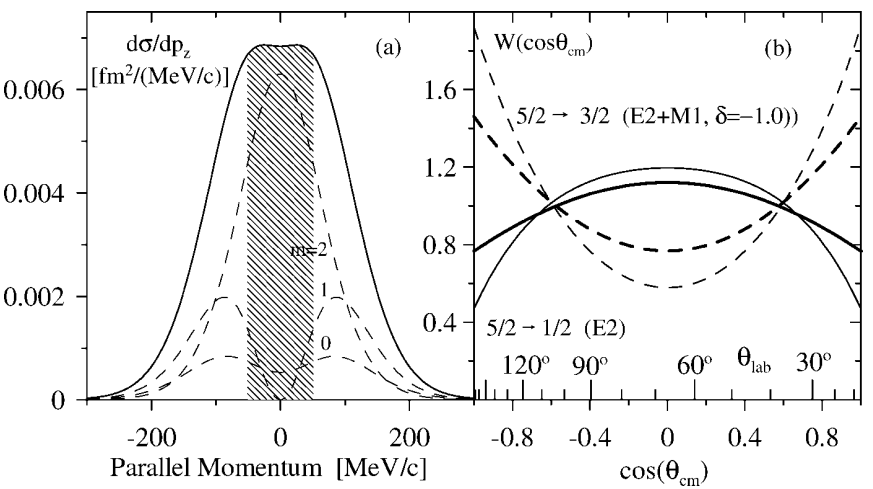

Figure 12 (*a*) The calculated longitudinal momentum distribution for the knockout of a $0d_{5/2}$ neutron in the ^{9}Be(^{28}Mg, ^{27}Mg)X reaction at 82 MeV/nucleon. The dashed lines give the contributions of the individual m_ℓ magnetic substates. A cut of ± 50 MeV/c increases the contribution of $m_\ell = \pm 2$ from 59 to 84% with 38% of the intensity included. (*b*) The calculated angular distributions for two possible spin sequences from the $5/2^+$ excited state of the residue. Dashed lines represent the $5/2 \rightarrow 3/2$ transition; solid curves are for $5/2 \rightarrow 1/2$. The gamma-ray angle relative to the beam axis in the center-of-mass frame is denoted $\theta_{\rm cm}$. The thick lines are for coincidences with all residues. The anisotropy is almost doubled (thin lines) by selecting central momenta of the cross-hatched area in (*a*). The upper scale on the *x*-axis shows the corresponding laboratory angles for a beam energy of 82 MeV/nucleon.

rates. However, at these forward angles, neutrons and charged particles generate a serious background in coincidence with the residues, and thus a better determination of the anisotropy may come from laboratory angles near 150°. The price, at the energy of this example, is an approximately fivefold reduction in the count rate per unit detector solid angle when compared with measurements at the forward angles. An alternative method would be to determine the angular correlation of the gamma ray with respect to the recoil direction of the residue in the center-of-mass system. The reconstruction of this would be technically demanding but would offer a very clear signature that would cover, in principle, the complete angular range, similar to the study of the neutron angular correlation from recoiling excited states of ^{10}Li cited in Figure 8.

Although it is beyond the scope of the present article, we mention for completeness the possibility of producing polarized nuclei using breakup reactions. Polarization here refers to different populations of the $+m$ and $-m$ magnetic substates. The seminal work of Asahi et al. (114) shows that polarized samples result if the residues are collected off the incident beam direction. The momentum selection is important (115); settings below and above the beam velocity typically give the largest values, the polarization changing sign in between. In these experiments, the residues were collected in a stopper and the polarization was detected using the asymmetry of the beta emissions. Combined with nuclear magnetic resonance techniques, the method is a powerful tool for measuring nuclear magnetic moments (116, 117). Breakup reactions must also be expected to produce alignment, although we lack the means to predict the magnitude of the effect. The observation of anisotropic angular distributions (118) for some gamma rays emitted from fragments with masses $A = 40$–45 following ^{48}Ca breakup at 60 MeV/nucleon provides a first qualitative indication of an alignment effect.

6. CONCLUDING REMARKS AND OPEN QUESTIONS

Direct-reaction spectroscopy of rare nuclei produced as weak, intermediate-energy fragmentation beams is still very young. Before summarizing what has been achieved, we enumerate some outstanding experimental and theoretical questions and challenges.

6.1. Open Experimental and Theoretical Questions

1. This article has emphasized *p-sd* shell nuclei, for which structure theory is advanced and sophisticated. This has been crucial to our understanding of the reliability of the reaction aspects of the analyses. Extending experiments into the *f-p* shells, and maybe beyond, is the logical next step. The corresponding mass region, approximately $A = 40$–100, represents the cutting edge of modern shell-model theoretical predictions, and a coordinated input of new and precise data will be both demanding and very rewarding.
2. Conclusions regarding the spectroscopic-factor reduction factors R_s, ascribed to short-range correlations, are based on a small data set and must

be regarded as provisional. More cases for configurations that are well understood (such as closed shell or halo systems) are needed to extricate these effects from those of long-range correlations. Experiments using calcium and nickel isotopes and their neighbors seem to be the logical starting point. Systematic measurements at several energies, maybe up to 1 GeV/nucleon, will be an important test of the accuracy and consistency of results. Theory provides some understanding of the R_s values of 0.5–0.65 observed for strongly bound orbitals. Can it also account for the values closer to unity found for halo cases?

3. The two-nucleon knockout reaction deserves much further effort, both experimentally and theoretically. The structure and reaction dynamics are entangled, and the spectroscopy will be both richer and more complex than in the case of single-nucleon knockout. The initial experimental results are a considerable stimulus to develop an integrated shell-model and reaction theory.
4. Alignment effects, both in the secondary beam and of the residues from knockout, pose a number of important questions. The model estimates of these effects discussed in this article have yet to be observed experimentally. How important are they, and how can they best be exploited for beam and reaction diagnostics and for an enhanced spectroscopy?
5. The expected deviations from the eikonal reaction theory have already been observed in selected reactions. Further, precision studies of these effects, theoretical as well as experimental, are important to understand quantitatively the limits with which cross sections, and hence absolute spectroscopic factors, can be deduced, and to gain further insight into the reaction mechanisms.
6. A potentially serious problem is posed by the presence of isomeric final states of the residue, for which the coincidence method fails. It will become necessary to develop techniques that can "flag" these cases. Similarly, the related uncertainty of isomeric components in the incident secondary beam, and their poisoning of the single- and two-nucleon spectroscopic studies, will need to be addressed.
7. A more systematic study of dynamical excitation of the residues, i.e., nonspectator effects, is also necessary. Single-particle excitations are unlikely to play any significant role, but collective (vibrational and rotational) excitations have already been suggested to be important in specific instances. A documented case (9) is the strength of the observed partial cross section of the ^{10}Be 2^+ state in neutron removal from ^{11}Be. Additional theoretical work must extend the reaction theory beyond the spectator core approximation.

6.2. Summing Up

The single-nucleon knockout reaction is becoming a major, efficient tool for the spectroscopy of single-particle states in light and medium-mass nuclei produced as fast radioactive beams. The method has three essential technical elements: a

fragment separator, which delivers the exotic species of interest on a light target; a high-resolution spectrograph, which identifies the reaction residues; and, operated in coincidence with the spectrograph, an array of gamma-ray detectors, which tag the individual residue excited-state populations following the reaction. Based on this information, partial cross sections and their longitudinal momentum distributions can be measured. The technique is very sensitive; experiments have used incident beams as sparse as one atom per second. The analysis of the spectral information uses a nonperturbative reaction theory, which is based on the sudden and eikonal approximations and requires a small, quite well-determined parameter set. This permits orbital angular-momentum assignments (from the shapes of the measured momentum distributions) and deduced spectroscopic factors (from the absolute partial cross sections). The cases studied so far show consistent agreement between experiment and theory at a level rivaling that of classical light-ion transfer reactions at tandem accelerator energies.

Although based on a limited number of cases, the new development discussed in Section 4 indicates that the knockout method can determine absolute spectroscopic factors. It confirms the quenching factors R_s of 0.5–0.65 for deeply bound proton states and obtains the same values for deeply bound neutron states, a new but not surprising result. This reduction, relative to shell-model calculations with effective interactions, is taken to be a manifestation of effects that go beyond these models. It is interesting that the less-bound states of radioactive nuclei have R_s values much closer to unity. Another significant step forward is the identification of two-proton knockout from neutron-rich systems as a direct reaction. This process, and two-neutron knockout on proton-rich nuclei, is very interesting. It leads away from stability toward extremely rare nuclei, offering a sensitive probe of excited states and, potentially, of correlations in the many-body nuclear wave function. The practical exploitation of this coherence of the two-nucleon knockout mechanism is a challenge for future experiments and theoretical structure and reaction studies.

ACKNOWLEDGMENTS

This work was supported by the U.S. National Science Foundation under Grant No. PHY-01 10253 and by the United Kingdom Engineering and Physical Sciences Research Council (EPSRC) Grant No. GR/M82141.

The *Annual Review of Nuclear and Particle Science* is online at http://nucl.annualreviews.org

LITERATURE CITED

1. Brown BA, Wildenthal BH. *Annu. Rev. Nucl. Part. Sci.* 38:29 (1988)
2. Brown BA. *Prog. Part. Nucl. Phys.* 47:517 (2001)
3. Otsuka T, Honma M, Mizuzaki T, Shimizu N, Utsuno Y. *Prog. Part. Nucl. Phys.* 47:319 (2001)
4. Honma M, Otsuka T, Brown BA, Mizuzaki T. *Phys. Rev. C* 61:064609 (2000)

5. Pieper SC, Wiringa RB. *Annu. Rev. Nucl. Part. Sci.* 51:53 (2001)
6. Glasmacher T. *Annu. Rev. Nucl. Part. Sci.* 48:1 (1998)
7. Navin A, et al. *Phys. Rev. Lett.* 81:5089 (1998)
8. Tostevin JA. *J. Phys. G* 25:735 (1999)
9. Aumann T, et al. *Phys. Rev. Lett.* 84:35 (2000)
10. Navin A, et al. *Phys. Rev. Lett.* 85:266 (2000)
11. Guimarães V, et al. *Phys. Rev. C* 61:064609 (2000)
12. Maddalena V, et al. *Phys. Rev. C* 63:024613 (2001)
13. Tostevin JA. *Nucl. Phys.* A682:320c (2001)
14. Hansen PG, Sherrill BM. *Nucl. Phys.* A693:133 (2001)
15. Enders J, et al. *Phys. Rev. C* 65:034318 (2002)
16. Tostevin JA, et al. *Phys. Rev. C* 66:024607 (2002)
17. Brown BA, Hansen PG, Sherrill BM, Tostevin JA. *Phys. Rev. C* 65:061601(R) (2002)
18. Enders J, et al. *Phys. Rev. C.* 67:064301 (2003)
19. Esbensen H. See Ref. (60), p. 71
20. Austin S. See Ref. (60), p. 42
21. Austern N. *Direct Nuclear Reaction Theories.* New York: Wiley (1970)
22. Macfarlane MH, Schiffer JP. In *Nuclear Spectroscopy and Reactions, Part B*, ed. J Cerny, p. 169. New York: Academic (1974)
23. Glendenning NK. In *Nuclear Spectroscopy and Reactions, Part D*, ed. J Cerny, p. 319. New York: Academic (1974)
24. Satchler GR. *Direct Nuclear Reactions.* Oxford, UK: Oxford Univ. Press (1983)
25. Feshbach H. *Theoretical Nuclear Physics: Nuclear Reactions*, p. 455. New York: Wiley (1992)
26. Johnson RC, Soper PJR. *Phys. Rev. C* 1:976 (1970)
27. Harvey JD, Johnson RC. *Phys. Rev. C* 3:636 (1971)
28. Kamimura M, et al. *Prog. Theor. Phys. Suppl.* 89:1 (1986)
29. Austern N, et al. *Phys. Rep.* 154:125 (1987)
30. Dieperink AEL, de Forest T. *Phys. Rev. C* 10:533 (1974)
31. Endt PM. *At. Data Nucl. Data Tables* 19:23 (1977)
32. Fortier S, et al. *Phys. Lett.* B461:22 (1999)
33. Winfield JS, et al. *Nucl. Phys.* A683:48 (2001)
34. Rehm KE, et al. *Phys. Rev. Lett.* 80:676 (1998); *Nucl. Instrum. Methods A* 449:208 (2000)
35. Korsheninnikov AA, et al. *Phys. Rev. Lett.* 82:3581 (1999)
36. Mukhamedzhanov AM, Timofeyuk NK. *JETP Lett.* 51:282 (1990)
37. Trache L, Carstoiu F, Gagliardi CA, Tribble RE. *Phys. Rev. Lett.* 87:271102 (2001)
38. Xu HM, Gagliardi CA, Tribble RE, Mukhamedzhanov AM, Timofeuk NK. *Phys. Rev. Lett.* 73:2027 (1994)
39. Beaumel D, et al. *Phys. Lett.* B514:226 (2001)
40. Gagliardi CA, et al. *Phys. Rev. C* 59:1149 (1999)
41. Smith GR, et al. *Phys. Rev. C* 30:593 (1984)
42. Jacob G, Maris TAJ. *Rev. Mod. Phys.* 38:121 (1966)
43. Kitching P, McDonald WJ, Maris TAJ, Vasconcellos CAZ. *Adv. Nucl. Phys.* 15:43 (1985)
44. Kramer GJ, Blok HP, Lapikas L. *Nucl. Phys.* A679:267 (2001)
45. Pandharipande VR, Sick I, de Witt Huberts PKA. *Rev. Mod. Phys.* 69:981 (1997)
46. Lapikas L, Wesseling J, Wiringa RB. *Phys. Rev. Lett.* 82:4404 (1999)
47. Hansen PG. *Nucl. Phys. News* 11(4):31 (2001)
48. Forsling W, Herrlander CJ, Ryde H, ed. *Proc. Int. Symp. Why and How Should We Investigate Nuclides Far Off the*

Stability Line, Lysekil 1966. Stockholm: Almqvist & Wiksell (1966); reprinted in *Arkiv för Fysik* 36:1 (Spec. issue) (1967)
49. Tanihata I, et al. *Phys. Rev. Lett.* 55:2676 (1985); *Phys. Lett.* B160:380 (1985)
50. Tanihata I, ed. *Research Opportunities with Accelerated Beams of Radioactive Ions. Nucl. Phys.* A693:1 (Spec. issue) (2001)
51. Kobayashi T, et al. *Phys. Rev. Lett.* 60:2599 (1988)
52. Orr NA, et al. *Phys. Rev. Lett.* 69:2050 (1992)
53. Bazin D, Caggiano JA, Sherrill BM, Yurkon J, Zeller A. *Nucl. Instrum. Methods B.* 204:90 (2003)
54. Glauber RJ. In *Lectures in Theoretical Physics*, ed. WE Brittin, 1:315. New York: Interscience (1959)
55. Bertulani CA, et al. *Physics of Radioactive Beams.* Nova Sci. (2002)
56. Thompson IJ, Suzuki Y. See Ref. (50), p. 424
57. Hansen PG, Jonson B. *Europhys. Lett.* 4:409 (1987)
58. Hansen PG, Jensen AS, Jonson B. *Annu. Rev. Nucl. Part. Sci.* 45:505 (1995)
59. Jonson B, Riisager K. *Phil. Trans. R. Soc. Lond. Ser. A* 358:2063 (1998)
60. Broglia RA, Hansen PG, eds. *Int. School of Heavy-Ion Physics, 4th Course: Exotic Nuclei*, p. 1. Singapore: World Sci. (1998)
61. Brown BA, Hansen PG. *Phys. Lett.* B381:391 (1996)
62. Hansen PG. In *Proc. Int. Conf. Exotic Nuclei and Atomic Masses, Arles, France, June 1995*, ed. M de Saint Simon, O Sorlin, p. 175. Orsay: Ed. Frontières (1995)
63. Hansen PG. *Phys. Rev. Lett.* 77:1016 (1996)
64. Esbensen H. *Phys. Rev. C* 53:2007 (1996)
65. Orr N. *Nucl. Phys. A* 616:155c (1997)
66. Hardy JC, Carraz LC, Jonson B, Hansen PG. *Phys. Lett.* B136:331 (1984)
67. Gottfried K. *Quantum Mechanics*, p. 113. New York: Benjamin (1966)
68. Bazin D, et al. *Phys. Rev. C* 57:2156 (1998)
69. Hussein M, McVoy K. *Nucl. Phys.* A445:124 (1985)
70. Hencken K, Bertsch G, Esbensen H. *Phys. Rev. C* 54:3043 (1996)
71. Al-Khalili JS, Tostevin JA, Thompson IJ. *Phys. Rev. C* 54:1843 (1996)
72. Tostevin JA, Al-Khalili JS. *Nucl. Phys.* A616:418c (1997)
73. Anne R, et al. *Nucl. Phys.* A575:125 (1994)
74. Charagi SK, Gupta SK. *Phys. Rev. C* 41:1610 (1990)
75. Ray L. *Phys. Rev. C* 20:1857 (1979)
76. Kox S, et al. *Phys. Rev. C* 35:1678 (1987)
77. Renberg PU, et al. *Nucl. Phys.* A183:81 (1972)
78. Ozawa A, Suzuki T, Tanihata I. *Nucl. Phys.* A693:32 (2001)
79. Typel S, Baur G. *Phys. Rev. C* 50:2104 (1994)
80. Warburton EK, Brown BA. *Phys. Rev. C* 46:923 (1992)
81. Iwasaki H, et al. *Phys. Lett.* B481:7 (2000); *Phys. Lett.* B 491:8 (2000)
81a. Maddalena V, Shyam R. *Phys. Rev. C* 63:051601 (2001)
82. Datta Pramanik U, et al. *Phys. Lett.* B551:63 (2003)
83. Cortina-Gil D, et al. *Phys. Lett.* B529:36 (2002)
84. Sauvan E, et al. *Phys. Lett.* B491:1 (2000)
85. Al-Khalili JS, et al. *Nucl. Phys.* A581:331 (1995)
86. Esbensen H, Bertsch GF. *Phys. Rev. C* 64:014608 (2001)
87. Esbensen H, Bertsch GF. *Nucl. Phys.* A600:37 (1995)
88. Brooke JM, et al. *Phys. Rev. C* 59:1560 (1999)
89. Tostevin JA, et al. *Prog. Theor. Phys. Suppl.* 146:338 (2003)
90. Bonaccorso A, Brink DM. *Phys. Rev. C* 38:1776 (1988)

91. Hasan H, Brink DM. *J. Phys. G* 4:1573 (1978)
92. Bonaccorso A. *Phys. Rev. C* 60:054604 (1999)
93. Bonaccorso A, Bertsch GF. *Phys. Rev. C* 63:044604 (2000)
94. Tostevin JA, et al. *Phys. Rev. C* 63:024617 (2001)
95. Chen L, et al. *Phys. Lett.* B505:21 (2001)
96. Chartier M, et al. *Phys. Lett.* B510:24 (2001)
97. Thoennessen M, et al. *Phys. Rev. C* 59:111 (1999)
98. Seth KK, et al. *Phys. Rev. Lett.* 58:1930 (1987)
99. Bohlen HG, et al. *Z. Phys. A* 330:227 (1988)
100. von Oertzen W, et al. *Nucl. Phys.* A588:129c (1995)
101. Hansen PG. *Nucl. Phys.* A682:310c (2001)
102. Simon H. *Phys. Rev. Lett.* 83:496 (1999)
103. Markenroth K, et al. *Nucl. Phys.* A679: 462 (2001)
104. Trache L, Carstoiu F, Mukhamedzhanov AM, Tribble RE. *Phys. Rev. C* 66:035801 (2002)
105. Olson DL, et al. *Phys. Rev. C* 28:1602 (1983)
106. Kidd JM, et al. *Phys. Rev. C* 37:2613 (1988)
107. Schwab W, et al. *Z. Phys. A* 350:283 (1995)
108. Blank B, et al. *Nucl. Phys.* A624:242 (1997)
109. Cortina-Gil D, et al. *Eur. Phys. J. A* 10:49 (2001)
110. Bazin D, et al. *Phys. Rev. Lett.* 91:012501 (2003)
111. Bohr Å, Mottelson BR. *Nuclear Structure*, Vol. 2, pp. 258–61, 641–46. New York: Benjamin (1975)
112. Johnson RC, Tostevin JA. *Spins in Nuclear and Hadronic Reactions*, p. 155. Singapore: World Sci. (2000)
113. Yamazaki T. *Nuclear Data* A3:1 (1967)

113a. Stuchberry AE. *Nucl. Phys. A* 723:69 (2003)

114. Asahi K, et al. *Phys. Lett.* B251:488 (1990)
115. Okuno H, et al. *Phys. Lett.* B335:29 (1994)
116. Mantica PF, et al. *Phys. Rev. C* 55:2501 (1997)
117. Rogers WF, et al. *Phys. Rev. C* 62:044312 (2000)
118. Sohler D, et al. *Phys. Rev. C* 66:054302 (2002)